REPORT DOCUMENTATION PAGE

Form Approved
OMB No. 0704-0188

1. REPORT DATE *(DD-MM-YYYY)*	2. REPORT TYPE	3. DATES COVERED *(From - To)*
06/30/2009	Final Technical Report	April 1, 2007 thru March 31, 2009

4. TITLE AND SUBTITLE
Investigation of ELF Signals Associated With Mine Warfare: A University of Idaho and ARD Collaboration, Phase I

5a. CONTRACT NUMBER

5b. GRANT NUMBER
N00014-07-1-0811

5c. PROGRAM ELEMENT NUMBER

6. AUTHOR(S)
Young, Jeffrey L.

5d. PROJECT NUMBER

5e. TASK NUMBER

5f. WORK UNIT NUMBER

7. PERFORMING ORGANIZATION NAME(S) AND ADDRESS(ES)
University of Idaho, Office of Sponsored Programs
Morrill Hall Room 414
PO Box 443020
Moscow, ID 83844-3020

8. PERFORMING ORGANIZATION REPORT NUMBER

9. SPONSORING/MONITORING AGENCY NAME(S) AND ADDRESS(ES)
Office of Naval Research
One Liberty Center
875 N. Randolph Street, Suite 1425
Arlington, VA 22203-1995

10. SPONSOR/MONITOR'S ACRONYM(S)
ONR

11. SPONSORING/MONITORING AGENCY REPORT NUMBER
PR# 08PR03078-01

12. DISTRIBUTION AVAILABILITY STATEMENT
Unlimited

13. SUPPLEMENTARY NOTES

14. ABSTRACT
The questions that are being asked in this investigation are: 1) once an ELF signal is generated, how far does it propagate and still be detectable and 2) how can such signals be modeled, excited and measured? To this end, the scenario considered is one in which an ELF source of the electric or magnetic kind is located in or above water, such as a lake or ocean. This source stimulates an ELF signal that is free to propagate in the water and air, and is reflected by various material interfaces, say between the water and air, or between the water and the floor. For purposes of experimental demonstration, the investigation focuses on the scenario of ELF sources and signals in the context of Lake Pend Oreille, where the Acoustic Research Detachment (ARD, Bayview, Idaho) is located and entrusted with the necessary assets to perform validation measurements.

15. SUBJECT TERMS
ELF, Electric Ship, EM Propagation

16. SECURITY CLASSIFICATION OF:			17. LIMITATION OF ABSTRACT	18. NUMBER OF PAGES	19a. NAME OF RESPONSIBLE PERSON
a. REPORT	b. ABSTRACT	c. THIS PAGE	UU	68	Jeffrey L. Young
U	U	U			19b. TELEPONE NUMBER *(Include area code)* 208-885-6829

Final Report

Investigation of ELF Signals Associated with Mine Warfare: A University of Idaho and Acoustic Research Detachment Collaboration, Phase One

by

Jeffrey L. Young, Dennis Sullivan, Robert G. Olsen and Christopher L. Wagner

Primary Contact:
Jeffrey L. Young
MRC Institute/Electrical and Computer Engineering
University of Idaho
Moscow, ID 83844-1024
208-885-6829
jyoung@mrc.uidaho.edu

for

Mr. Dana W. Hesse
Program Officer
Office of Naval Research
875 N. Randolph Street, Suite 1425
Arlington VA 22203-1995
Voice: +1 703-696-8557 DSN 426-8557
Email: dana_hesse@onr.navy.mil

June 30, 2009

Supporting Information:

Contract Number: N00014-07-1-0811

Original Contract Period: April 1, 2007 through March 31, 2008
Extended Contract Period: April 1, 2008 through March 31, 2009

FY07 Funded Amount: $660,000

Introduction

Described herein are the key findings and results associated with the project entitled "Investigation of ELF Signals Associated with Mine Warfare, A University of Idaho and Acoustic Research Detachment Collaboration, Phase One." Extremely low frequency (ELF) electromagnetic signals are used by enemy combatants to detect and, subsequently, to incapacitate, by means of surface and subsurface mines, naval vessels. This program is of high importance to the Navy – particularly since ELF signals are one of the primary signature emissions of the Navy's proposed electric ship fleet.

In principle, the questions that are being asked in this investigation are: 1) once an ELF signal is generated, how far does it propagate and still be detectable and 2) how can such signals be modeled, excited and measured? To this end, the scenario considered is one in which an ELF source of the electric or magnetic kind is located in or above water, such as a lake or ocean. This source stimulates an ELF signal that is free to propagate in the water and air, and is reflected by various material interfaces, say between the water and air, or between the water and the floor. For purposes of experimental demonstration, the investigation focuses on the scenario of ELF sources and signals in the context of Lake Pend Oreille, where the Acoustic Research Detachment (ARD, Bayview, Idaho) is located and entrusted with the necessary assets to perform validation measurements.

The research program was designed with two major thrusts: Modeling and experimentation. The modeling thrust was coordinated and executed by the University of Idaho (UI), Moscow, Idaho; the experimentation thrust was coordinated and executed by ARD. This report focuses primarily on the modeling thrust. A separate report from ARD will be issued that addresses the experimentation thrust.

ELF Modeling

Modeling of ELF electromagnetic signals in water environments can be accomplished either by means of direct, analytical solution of Maxwell's equations or by numerical solutions of the same. The former is attractive for purposes of gaining insights into the physical mechanisms that hinder or aid the propagation of ELF signals. The disadvantage is found in the number of simplifying assumptions that are made to bring about a closed-form solution. A numerical solution has no such simplifying assumptions, but does suffer from discretization errors. In principle, it can model all of the physical and geometrical features of the domain of consideration. The price paid for doing so, however, is the required time and the CPU/memory resources needed to accomplish the task. Data visualization and management are other issues that need to be addressed when working with large data sets produced by numerical solvers. The positive and negative tradeoffs between these two approaches (i.e. analytical vs. numerical) suggest that no one method is superior. For that reason the

UI team adopted a diverse strategy that encompasses many different approaches in order to assure a positive outcome and to provide deliverable modeling methodologies.

The four principle techniques that were considered during the Phase One effort were the a) Sommerfeld Half-Space (SHS) method, b) Finite-difference, time-domain method (FDTD), c) High Frequency Structural Simulator (HFSS), finite-element method, and d) the quasi-static method (QS). A summary of these methods is provided next. Detailed information on each of them is provided in the attached appendices.

The SHS method is an analytical approach that assumes that all interfaces (say between water and air, or between water and floor) are planar and infinitely extended. This is assumption is reasonably valid for the water-air interface, particularly in open water regions where the source is located near the surface. For the littoral zones, the method may fail, particularly when electric sources are used to excite the ELF signals. By assuming that the interfaces are flat, a closed-form solution can be devised that is cast in terms of Fourier-Bessel integrals. These integrals can be evaluated numerically and rapidly in a matter of seconds on any desktop machine. Even with the potential deficiency of treating all interfaces as planar, the SHS method is attractive as a validation tool for the other numerical modeling approaches. For example, the team used the SHS method to validate the data produced by the FDTD or HFSS methods (described next) when these numerical methods consider the same layered media problem statement. Professor Robert Olsen of Washington State University (WSU) is the lead investigator of the SHS method.

The FDTD method is a numerical approach that discretizes Maxwell's equations in their fundamental form using a staggered grid and leap-frog integrator. This method has been fully vetted in the open literature and has been established as a robust way of obtaining accurate simulation data. In principle, the FDTD method accounts for all material interfaces and material inhomogeneities by assigning permittivity, permeability and conductivity values along edges of the grid elements. Curvilinear boundaries are approximated by straight line, stair-stepped boundaries. For geometrical features that are significantly less than a wavelength, such stair-stepping causes no appreciable errors in the computed data. The domain of interest at Lake Pend Oreille is about 8 km on a side; the lake floor at its deepest point is about 335 km. Assuming an operating frequency of 100 Hz and a water conductivity of 0.018 S/m, the corresponding skin depth is 375 m and the wavelength is 2.356 km; for air, the wavelength is 3,000 km. Thus the domain spans a fraction of a wavelength in air but about 3.4 wavelengths (or 21.3 skin depths) in water. The significant disparity between these two relative sizes potentially introduces computational complexities. One area of concern that was addressed in this project was the proper design of an absorbing boundary condition (ABC) or perfectly matched layer (PML) that will allow an open physical domain to be truncated into a finite computational domain.

Placement of this ABC/PML in terms of wavelengths is critical if non-spurious reflections are to be avoided. Typically, the farther an ABC is placed away from a scattering object, the better it performs. However, this increases the computational domain size and hence, increases the simulation time and CPU/memory requirements of the computer. PML's are more complex to implement, but can be placed closer to the scattering object while sustaining excellent absorption characteristics. Professor Dennis Sullivan of the University of Idaho is the lead engineer of the FDTD and PML effort.

HFSS is a commercially available electromagnetic, finite-element, frequency-domain, numerical solver that has been designed by Ansoft/Ansys for antenna and microwave circuit applications. One question that was asked in this investigation was whether such a tool could be used to predict the electromagnetic propagation characteristics of an ELF signal in a highly conductive environment. We believe that the answer is a qualified yes. However, being that the solver is commercial and not custom, the user does not have direct control over some of the solver's functionality. This is readily apparent in the method by which the ELF sources are constructed in the solver's graphical user interface (GUI). Second, some of its interpolation functions cause some errors in the outputted data. Third, learning how to import the geometrical features of the Lake into the solver and optimizing the corresponding computational mesh is needed. Hence, the team spent considerable amount of time wrestling with these issues, but the results generated to date seem favorable. Professor Jeffrey Young of the University of Idaho is the lead engineer of the HFSS effort.

The quasi-static method was also considered given the ELF nature of the electromagnetic signals. By definition, the quasi-static method does not consider any wavelike mechanisms in Maxwell's equations; it assumes that the field lines are the same as the static field, but oscillating. This is accomplished by neglecting a) electric displacement currents for magnetic sources and b) magnetic displacement currents for electric sources. By doing so, simple solutions can be constructed that correlate well with other more advanced solutions, like HFSS and FDTD. Professor Jeffrey Young of the University of Idaho is the lead engineer of the quasi-static modeling effort.

Each of the aforementioned numerical methods requires a precise understanding of the electrical and geometrical features of the Lake. To this end, the team spent considerable amount of time digitizing graphical topological and bathymetry data over an 8 km by 8 km region of the Lake that is centered on the electromagnetic array (EMA), as shown in Figure 1.

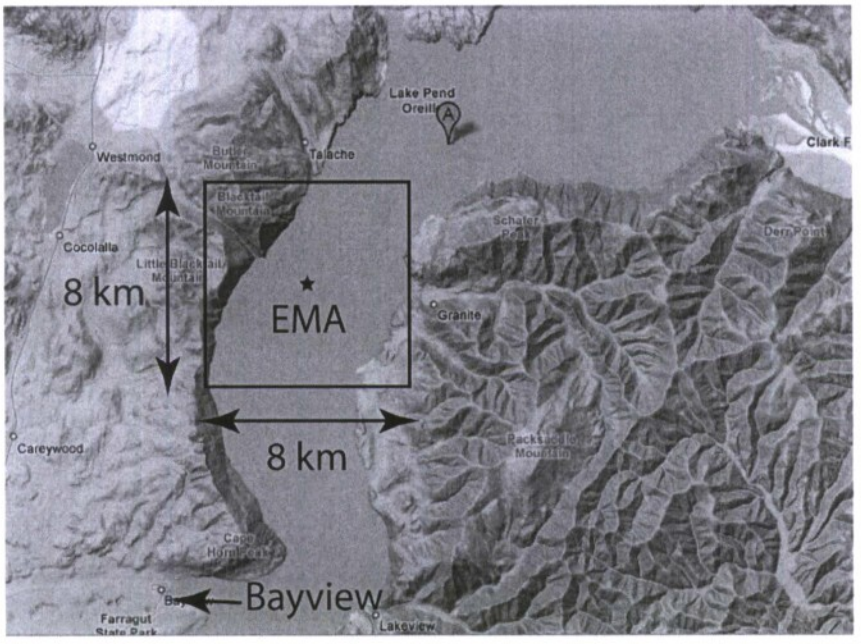

Figure 1: Electromagnetic domain of interest.

Renditions of the cross-sectional portion of the Lake, as obtained from this discretization process and starting from the north end of the Lake, are shown in Figures 2 through 5.

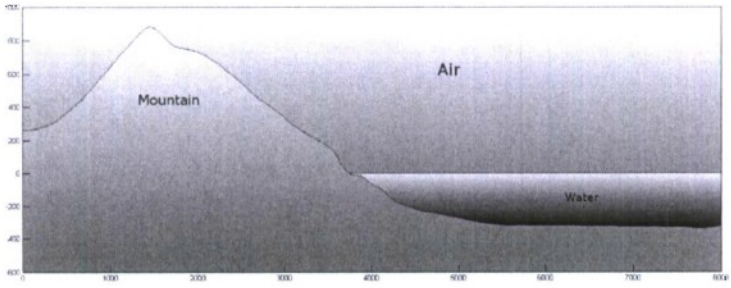

Figure 2: Cross-sectional rendering of the Lake; far-north end.

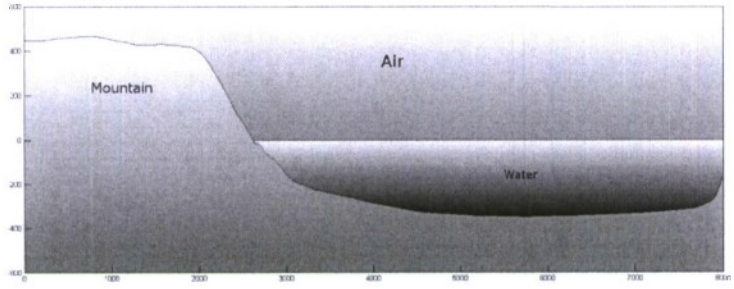

Figure 3: Cross-sectional rendering of the Lake; middle-north end.

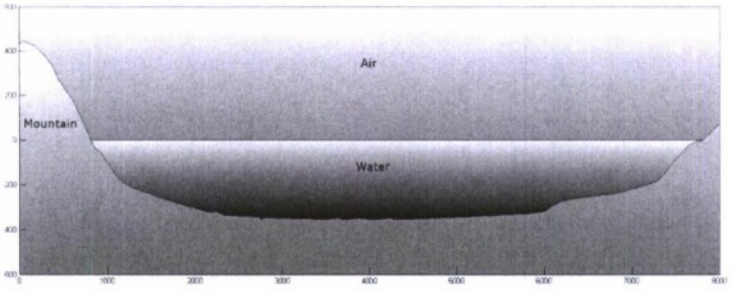

Figure 4: Cross-sectional rendering of the Lake; middle-south end.

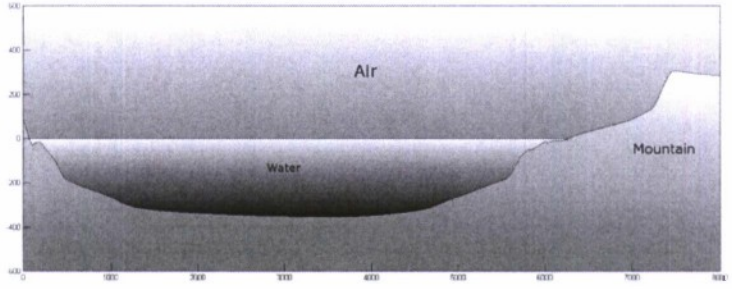

Figure 5: Cross-sectional rendering of the Lake; far-south end.

For these cross-sections, we see that the Lake spans about 6.5 km and has a depth of about 375 m; the highest land feature is about 425 m above the Lake. Once digitized and stored electronically, each of the previously discussed solvers could use that data in their computations.

In addition to precise geometrical data, the various solvers also require precise knowledge of the conductivity of the Lake and the mud at the bottom of the Lake. The UI team used a value of 0.018 S/m for the water and 0.012 S/m for the mud floor. The former number was previously measured by ARD; the latter number was measured during the course of Phase One by filling a PVC tube with the mud, placing electrodes on the ends of the tube as caps and measuring the total resistance between the electrodes. By knowing the geometrical dimensions of the tube, we were able to determine the conductivity from the resistance value. As for the value of the dielectric permittivity of the Lake, this was not deemed essential, since displacement currents in the Lake are virtually insignificant relative to the conduction currents.

Although detailed information pertaining to the experimental portion of this project will be documented by ARD, a few words about it are needed to set the context of how the models are validated. Most of the validation data that has been used to date was gathered in December 2008 by ARD. In one set of experiments, an electric source was devised by mounting two metallic plates on the hull of a boat (see Figure 6); in

another, one plate was attached to the boat, which also towed a skiff with the other metallic plate attached to it. The distance between the boat and the skiff was 40 meters.

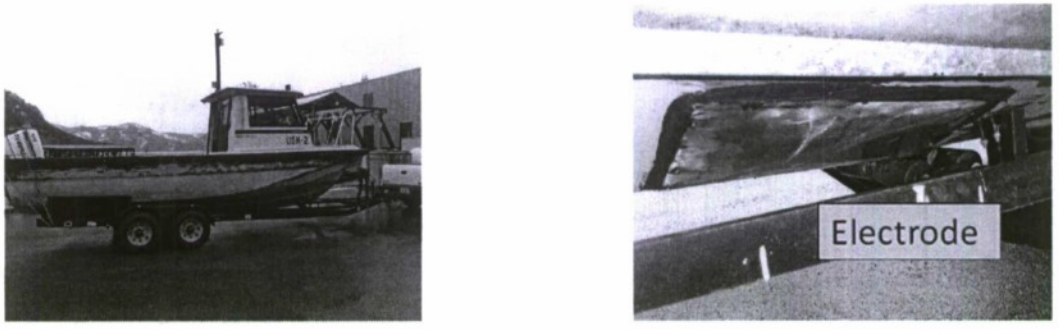

Figure 6: Electrodes on the source boat.

In both cases, the plates were connected to cables, which were also connected to a low-frequency, high-powered ELF signal source. For the case of the skiff, an ac electric current of 1.25 A passed through the plates allowing conduction currents to flow in the water. These currents stimulated both and magnetic fields within the Lake. As the boat motored across the Lake's surface, precise GPS data was logged to determine its position and heading. Over five days, about 225 runs were executed consisting of 85 noise/calibration runs and 140 experimental runs. The experimental runs for phase II are shown in Figure 7. Many of the boat runs were redundant.

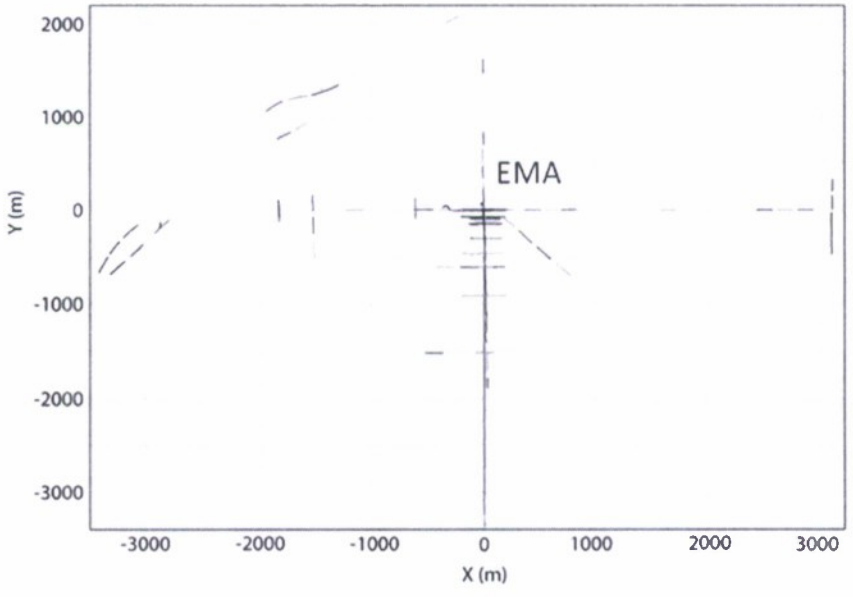

Figure 7: Experimental boats runs conducted by ARD in December 2008.

The grid of Figure 7 was rotated to match the alignment of the electromagnetic array (EMA, i.e. field sensing unit) thus making the x-axis shifted 10 degrees positive from that of easting. The alignment of the sensors can randomly shift up to 5 degrees during the measurement process, due to water motion. The range of the experiment was about 6.7 km in the x-direction and 5.6 km in the y-direction, or 37.5 km^2 with the EMA as the origin. Most of the experiment runs were perpendicular or transverse to an axis of the EMA and some were at arbitrary angles to it.

Of these 140 runs, about 25 of them have been processed. The average boat speeds of these runs were computed from the GPS and time-stamping data; several boat speeds are shown in Figure 8. From this plot, we see that the speeds are typically between one to three meters per second.

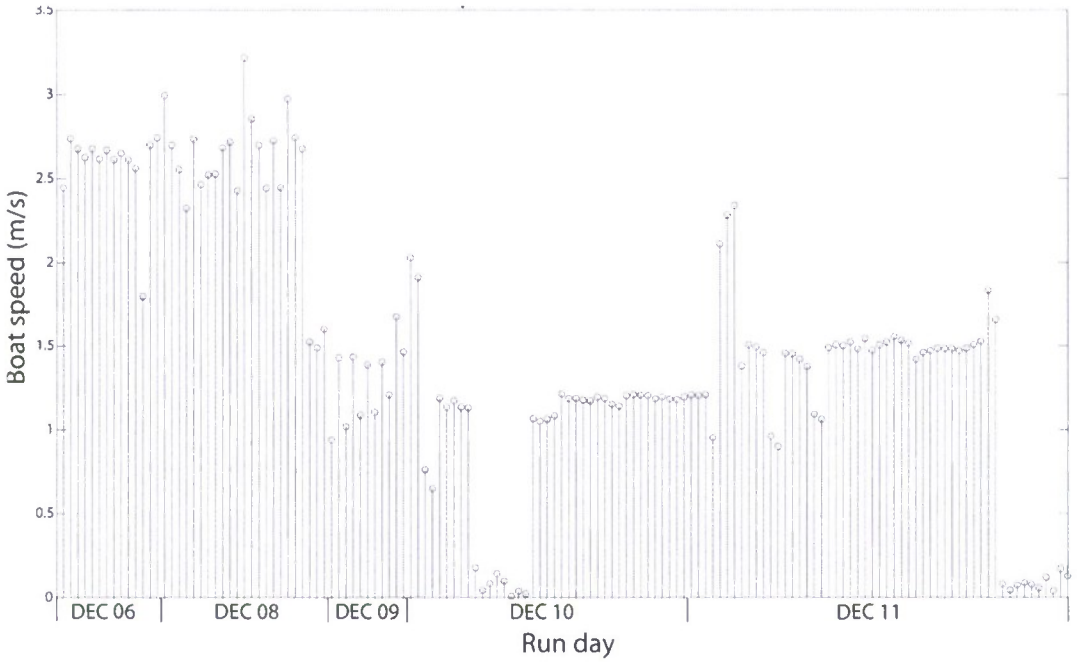

Figure 8: Boat speeds for various runs.

To detect the fields, a series of electric and magnetic sensors were connected to a truss unit called the electromagnetic array (EMA) (see Figures 9 and 10) that could be raised (or lowered) from the Lake floor to the surface by ARD's Target Modeling Hauler (TMH). The sensors were connected to a data acquisition system and field strength amplitudes were sampled 6,000 times per second, resulting in a Nyquist frequency of 3 kHz.

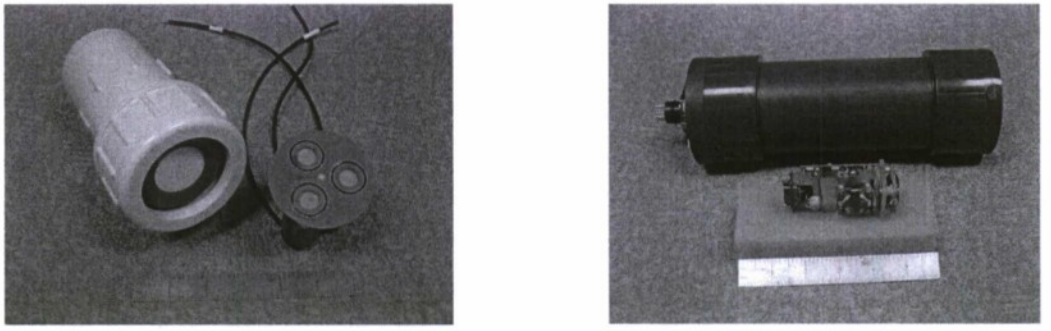

Figure 9: Electric (left) and magnetic (right) sensors.

Figure 10: Electromagnetic Array

Once the raw experimental data was gathered and recorded, a post-processing methodology had to be devised that could extract the ELF spectral component associated with the ELF source. This processing step required the use of a rectangular window function and Fast Fourier Transform (FFT) techniques operating on a one second sample of time-domain data (i.e. 6,000 samples). The other part of the post-processing step required the manipulation of the GPS data to match the coordinate systems of the FDTD, HFSS and QS models with the experiment. This step is not necessarily a complicated one, but care does need to be exercised to insure that the various coordinate axes are parallel and share a common origin. Several MatLab scripts have been written to handle both the FFT and GPS processing steps. A typical FFT spectrum from the experimental data is shown in Figure 11. The 100 Hz signal frequency is clearly seen, but is surrounded by a 60 Hz spectra and its plethora of harmonics. The noise floor is seen to be roughly 10 nV/m.

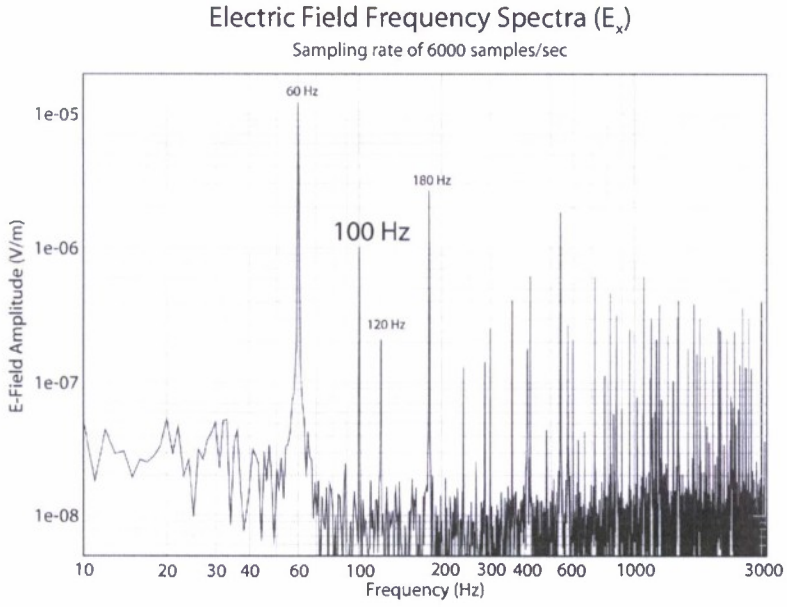

Figure 11: Typical spectrum of the experimental data.

It should be noted that the experiment was conducted by moving the source about the lake for a fixed observation point. The simulations were conducted under the assumption that the source is fixed and the observation points are free to move. Since the relative distance between the source and the observation points is the critical dimension and since the medium is reciprocal, reciprocity can be invoked to assure that both approaches generate identical data.

Key Results

In the attached appendices, several specific results are given for each method. However, many of these methods have been validated by each other and by experimental data. These key results are presented next.

First consider Figure 12, which shows the six test validation scenarios and boat paths.

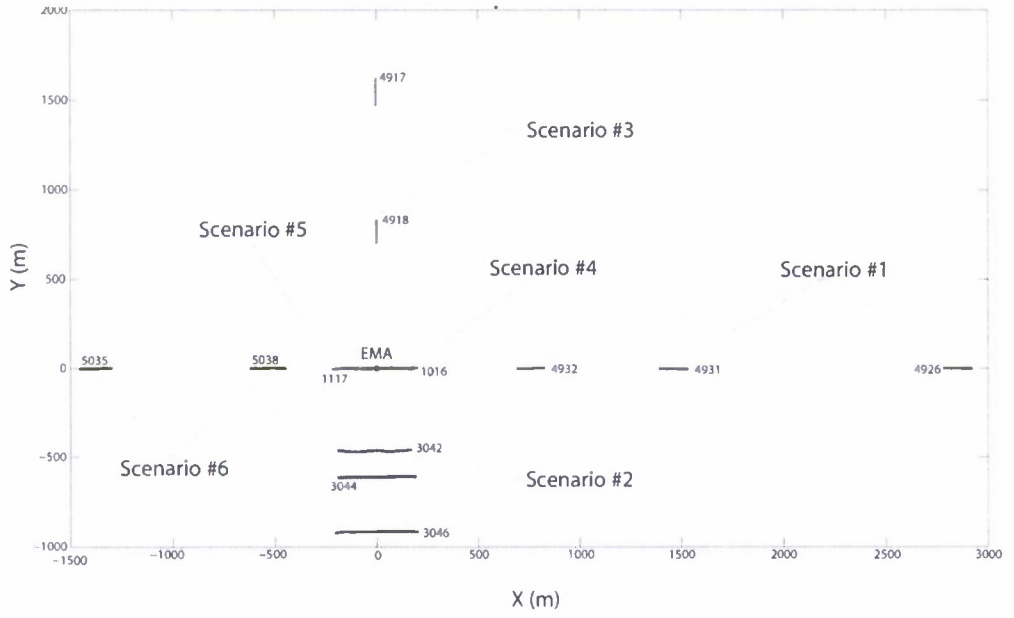

Figure 12: Six validation scenarios and the corresponding boat paths.

Data for these six scenarios are shown in Figures 13 through 19. A summary of this data is provided next.

- Figure 13: This corresponds to runs 4932, 4931 and 4926 for a 40 m, 1.25 A, 1,000 Hz electric source. Data from the quasi-static, Sommerfeld (i.e. WSU), FDTD and HFSS methods for the *x*-component of the electric field are plotted as a function of radial distance when the EMA is located at a depth of 8.23 m. All but the quasi-static method align very well with the experimental results. However, since this data corresponds to distances between 500 and 3,000 meters, which span multiple wavelengths at 1,000 Hz (i.e. λ=118 m), the quasi-static method is not appropriate for this test case. Even so, it still predicts the correct trend and is only off by a factor of two.

- Figure 14: This corresponds to runs 3046, 3044 and 3042 for a 40 m, 1.2 A, 100 Hz electric source. Data from the quasi-static, Sommerfeld (i.e. WSU), FDTD and HFSS methods for the *x*-component of the electric field are plotted as a function of radial distance when the EMA is located at a depth of 8.23 m. In this case, all methods fail to give the correct experimental value, but nevertheless come close to it. Since the WSU and FDTD methods predict the same data, we surmise that the error is associated with some imprecise parametric value in the experiment. Further investigation is needed for this case.

- Figure 15: This corresponds to runs 4917 and 4918 for a 40 m, 1.25 A, 1,000

Hz electric source. Data from the quasi-static, Sommerfeld (i.e. WSU), FDTD and HFSS methods for the *y*-component of the electric field are plotted as a function of radial distance when the EMA is located at a depth of 8.23 m. The exact same observations that were made for Figure 13 apply to this case.

- Figure 16: This corresponds to run 1016 for a 190 A-m^2, 10 Hz magnetic source. Data from the Sommerfeld (i.e. WSU), FDTD and HFSS methods for the *y*-component of the electric field are plotted as a function of radial distance when the EMA is located at a depth of 8.23 m. In this case the FDTD and Sommerfeld methods predict correctly the experimental outcome. HFSS predicts the correct trend, but the data are corrupted by random spikes. The cause of these spikes is understood. Since a magnetic source will weakly excite an electric field, the ability to compute such weak fields is strongly dependent on the HFSS mesh. Further work on mesh generation issues is needed.

- Figure 17: This also corresponds to run 1016 for a 190 A-m^2, 10 Hz magnetic source. Data from the Sommerfeld (i.e. WSU), FDTD and HFSS methods for the *z*-component of the magnetic field are plotted as a function of radial distance when the EMA is located at a depth of 8.23 m. In this case the FDTD and Sommerfeld methods predict the same outcome. HFSS also predicts the correct outcome, but there are some noticeable deviations from the experimental data. All three methods are in slight disagreement with the experimental data.

- Figure 18: This corresponds to run 1117 for a 0.5 A-m, 100 Hz electric source (i.e. both electrodes are on the same boat). Data from the quasi-static, Sommerfeld (i.e. WSU), FDTD and HFSS methods for the *x*- and z-components of the electric field are plotted as a function of radial distance when the EMA is located at a depth of 295 m. (Note: Two different FDTD codes were written for this scenario to gauge their relative robustness; the results are virtually the same.) Here we see that the data from all five methods generate virtually the same result. However, none of the methods correctly predict the dip in the experimental field data. The cause of this is due to positional ambiguity of the moving source. For close range observations (in this case 10 meters or so), the source could have moved several meters during the one second sampling interval, which suggests that its effective static position is unknown. Since several meters is a large fraction of 10 meters, this positional ambiguity is large. In earlier cases the observations were on the order of hundreds of meters and a positional ambiguity of a few meters is inconsequential. We also note the quasi-static method compares favorably to the experimental data, which is to be expected for such close range observations.

- Figure 19: This corresponds to runs 5035 and 5038 for a 50 A-m, 10 Hz electric source (i.e. both electrodes are on the same boat). Data from the quasi-static, Sommerfeld (i.e. WSU), FDTD and HFSS methods for the x- and z-components of the electric field are plotted as a function of radial distance when the EMA is located at a depth of 295 m. Since the dip in the field data occurs around 200 meters, the positional ambiguity effect, as noted previously, is not present. Also, we see that the FDTD data and the experimental data agree the best, although the other methods give reasonable results.

Recall that the experimental data is gathered in sets of one second sample bins. Each bin corresponds to an approximate location of the boat. The actual position of the boat is ambiguous due to a non-zero boat speed. Consider Figure 20, which shows the effect of using bin sample sizes in excess of one second. As the sampling interval increases, the expected outcome of smoother data is also seen. For long-range observations, the increase in sample bin sizes does not have an adverse effect on the data. This will not be case for close-range distances since a 10 second bin size will correspond to a 20 to 30 meter positional ambiguity of the source.

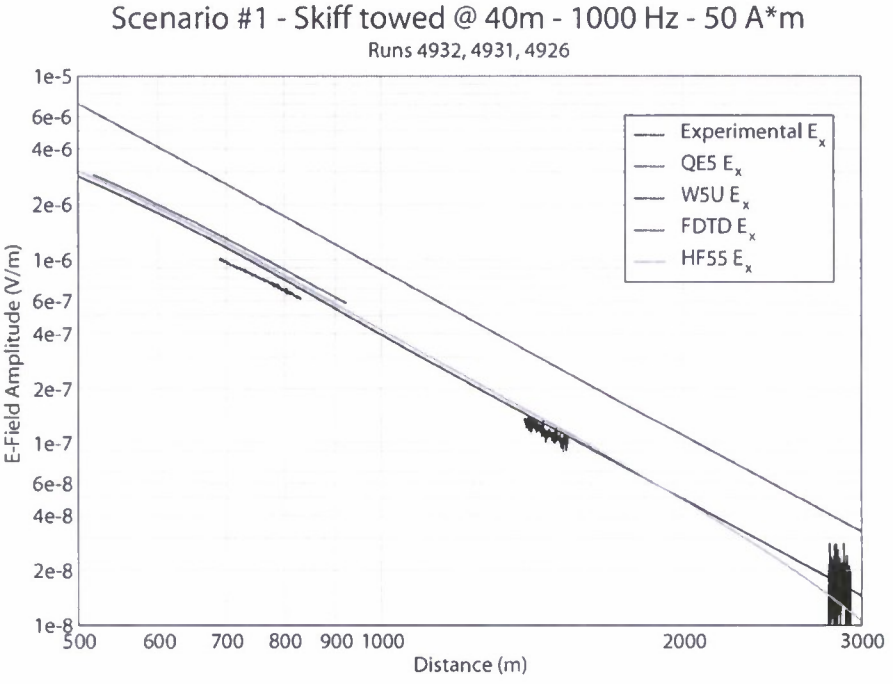

Figure 13

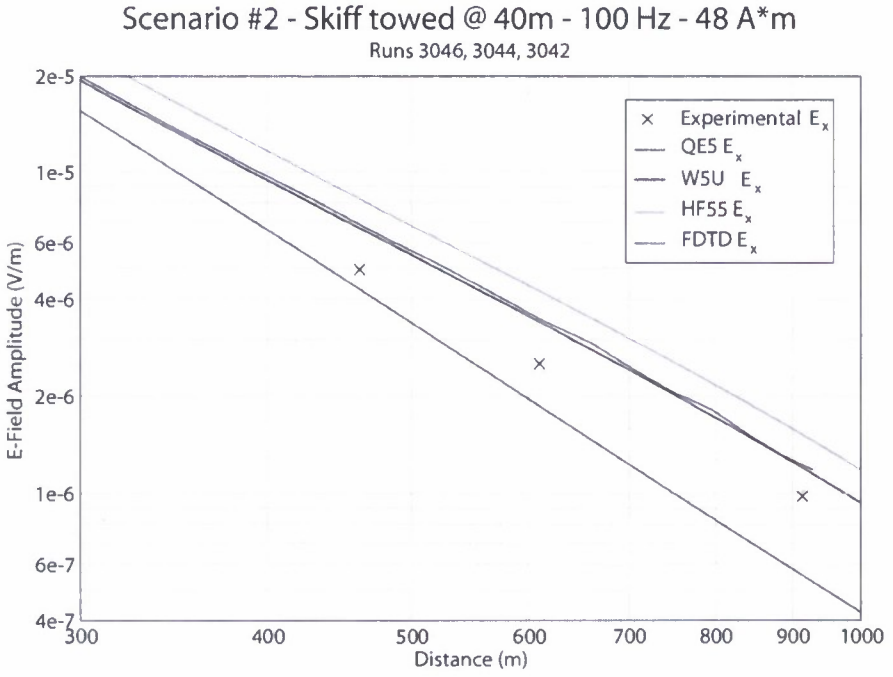

Figure 14

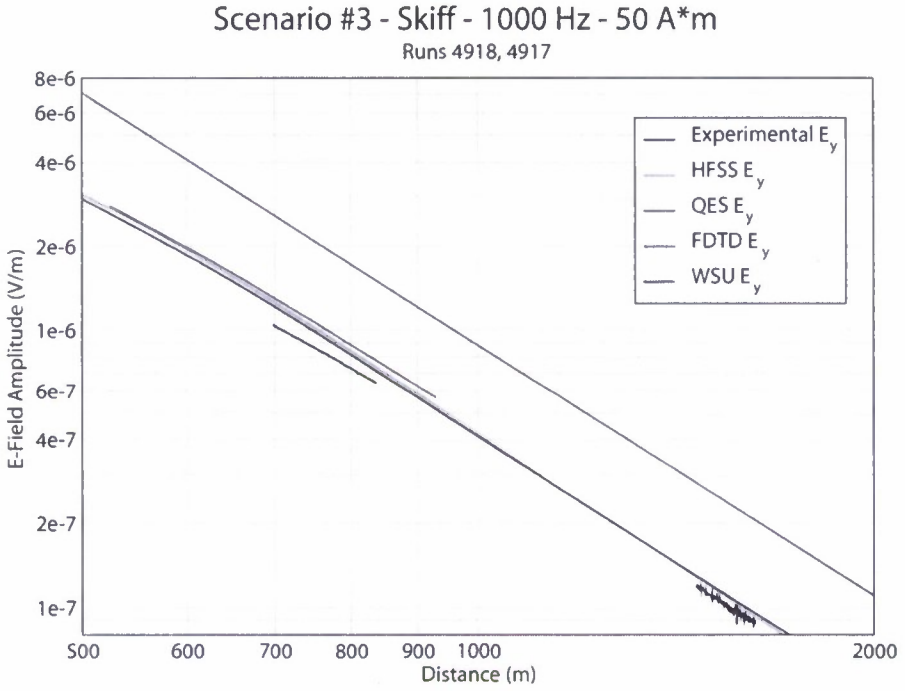

Figure 15

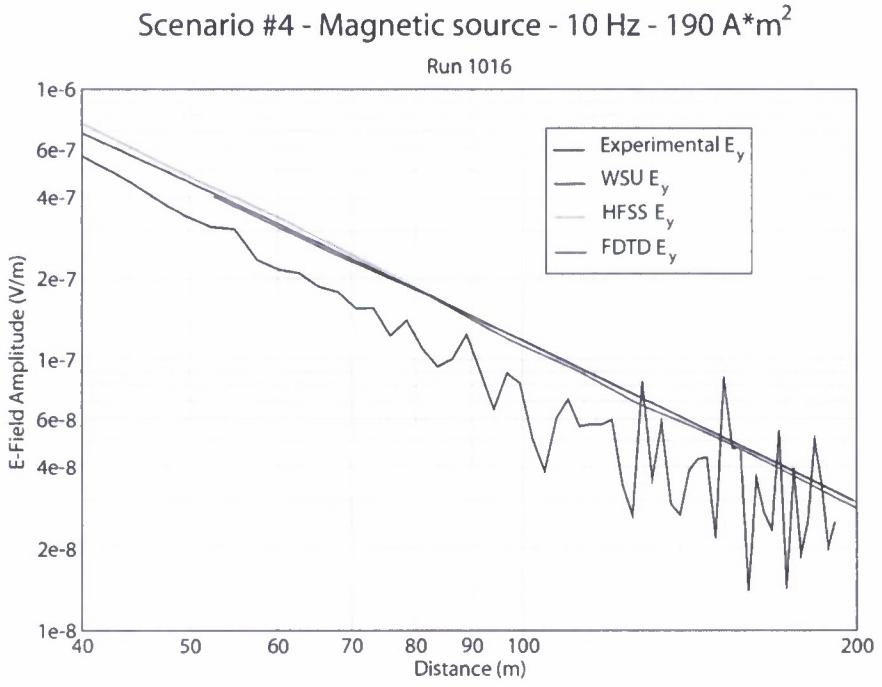

Figure 16

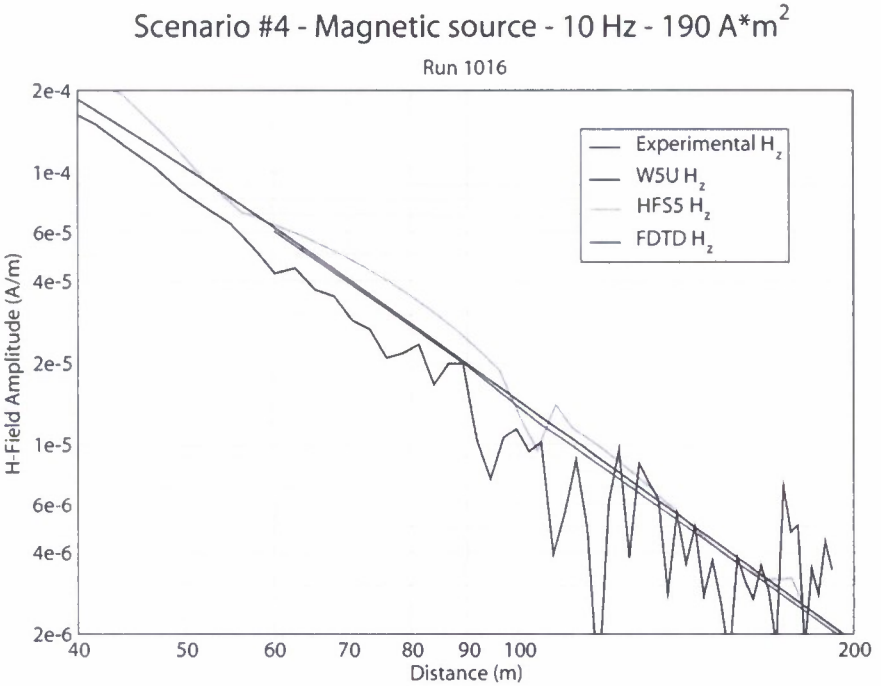

Figure 17

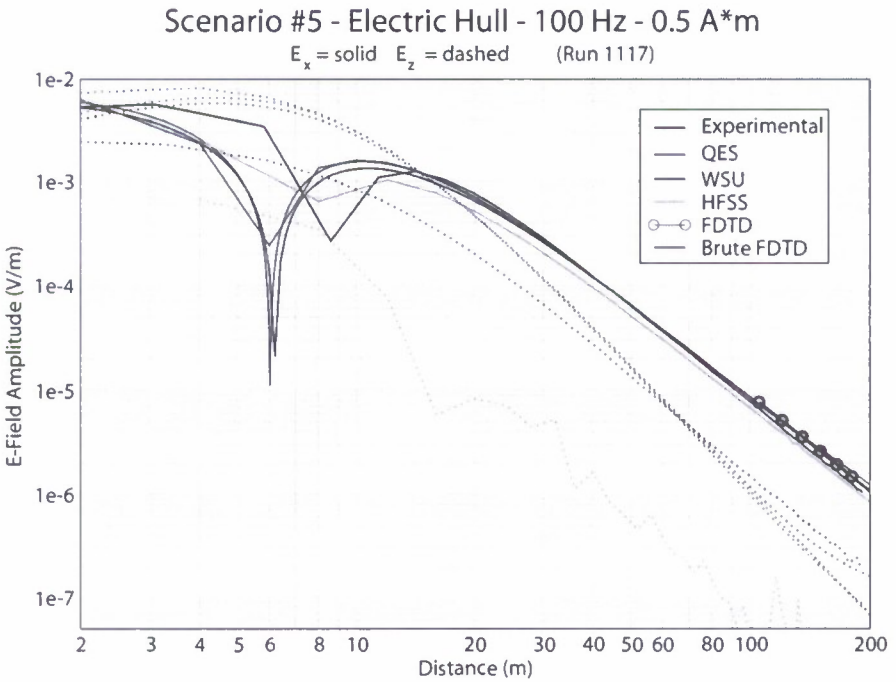

Figure 18

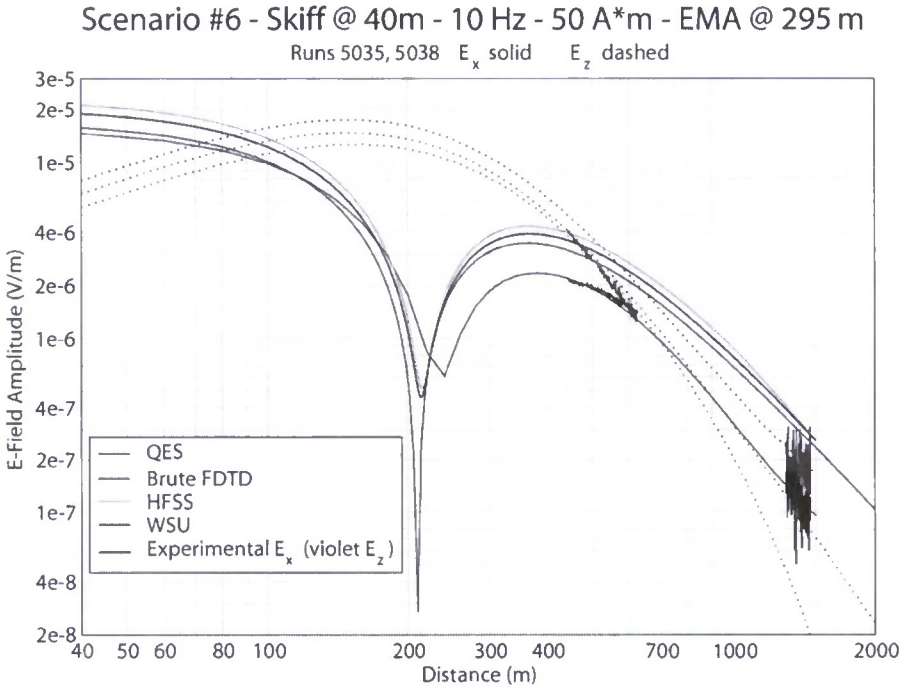

Figure 19

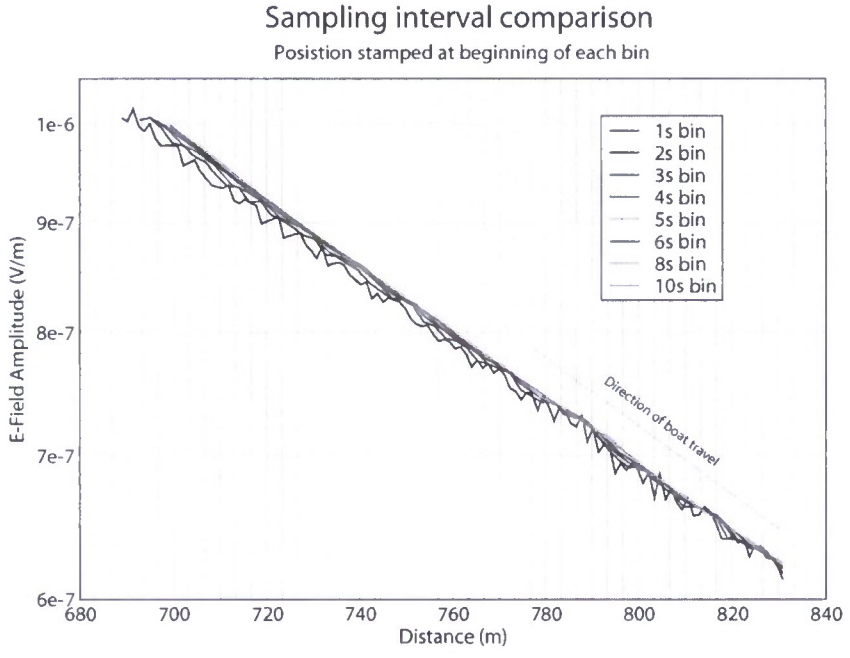

Figure 20

Future Work

Based on the previous discussions and the objectives of the project, the following future work is envisioned:

- HFSS predicts the correct result once a frequency-dependent calibration factor is specified. We surmise that this factor is related to the wave-number, since the factor is proportional to $f^{1/2}$. Work is needed to understand why this factor is needed and its precise relationship to frequency.
- There are two ways to implement a source in HFSS; each way has its advantages. We need to investigate whether Hertzian or scattered field sources are best.
- HFSS requires us to import Lake topographical and bathymetry data. Since the Lake floor, in particular, is smooth in some places and spatially varying in other places, we need to optimize the HFSS grid to these places to assure fast simulations and accurate data. Mesh optimization will be done with a specialized mesh editor from Sandia laboratories.
- HFSS introduces errors, particularly in the magnetic field calculation at ELF frequencies. This calculation can be improved by mesh refinement. More research is needed to figure out how the mesh should be refined.
- Boat motion errors associated with source position ambiguity are made manifest, particularly close to EMA. Further work is needed to account for this effect in the modeling software.
- FDTD results tend to be slow on single processor or single core machines. Multi-core FDTD optimization and parallelization of the FDTD codes will be implemented.
- Mesh truncation schemes for FDTD have been explored in Phase I. Further work in the area of perfectly matched layers is still needed.
- Ansys/Ansoft has a product called "Maxwell," which is a static field solver. Research is needed to see if this code can predict the quasi-static results.
- The Sommerfeld methodology has been shown to predict accurate results. One advantage of a closed-form solution is the ability to predict the up-over-down effect. This effect suggests that the up-over-down wave is less attenuated (with respect to the direct wave) once the wave escapes into the air medium. This analysis will be accomplished in Phase Two.
- An experiment in the Fall of 2009 and the Spring of 2010 is scheduled to produce more validation data.
- During Phase Three user manuals and documentation will be written for each of the delivered models and codes.

UI and WSU Team Members

- Prof. Jeffrey L. Young, Lead PI, UI
- Prof. Dennis Sullivan, Co-PI, UI
- Prof. Robert G. Olsen, Co-PI, WSU
- Dr. Christopher L. Wagner, Research Engineer, UI
- Mr. Yang Xia, Research Engineer, UI
- Mr. Robert Rebich, Graduate Research Assistant, UI
- Mr. Christopher Johnson, Graduate Research Assistant, UI
- Mr. Hang Dong, Graduate Research Assistant, UI
- Mr. Alireza Mansoori, Graduate Research Assistant, UI
- Mr. Zhi Li, Graduate Research Assistant, WSU
- Mr. Chenchen "Jimmy" Li, Undergraduate Research Assistant, UI

Publications:

- Y. Xia and D.M. Sullivan, "Underwater FDTD simulations at extremely low frequencies," *IEEE Antennas and Wireless Propagation Letters*, vol. 7, pp. 661-664, 2008.

- Y. Xia and D. M. Sullivan, Z. Li, and R. Olsen "Dual problem space FDTD simulation for underwater ELF applications," *IEEE Antennas and Wireless Propagation Letters*, vol. 8, 2009 (to be published).

- D. M. Sullivan and Y. Xia, "Underwater ELF simulation using the FDTD method," IEEE International Antennas and Propagation Symposium and USNC/URSI Radio Science Meeting, June 5-11, 2008, San Diego, CA.

- Y. Xia and D. M. Sullivan, "Near to far field transformation for underwater ELF simulation," IEEE International Antennas and Propagation Symposium and USNC/URSI Radio Science Meeting, June 5-11, 2008, San Diego, CA.

- Y. Xia, A. Monsoori, D. M. Sullivan and J. Nadobny, "High resolution interpolation for underwater FDTD simulation at ELF frequencies," IEEE International Antennas and Propagation Symposium and USNC/URSI Radio Science Meeting, June 1-5, 2009, Charleston, SC.

- Sullivan D. M., Xia Y., "A perfectly matched layer for lossy media at extremely low frequencies," IEEE International Antennas and Propagation Symposium and USNC/URSI Radio Science Meeting, June 1-5, 2009, Charleston, SC.

Master of Science Theses:

- Xia, Yang, "Three-dimensional FDTD simulation for underwater ELF signals," Master of Science in Electrical Engineering, University of Idaho, August, 2008

Appendix A: Sommerfeld Half Space Method

Robert G. Olsen, Zhi Li

School of Electrical Engineering & Computer Science, Washington State University

Formulation

The purpose of this project is to find analytical solutions for the electric and magnetic fields in any layer of a 3-layer non-magnetic media model when a vertical or horizontal magnetic dipole (VMD or HMD) is radiating in the middle layer. The three layers, from top to bottom, are assumed to be air, lake water and lake bottom. And they are denoted as layer #0, #1 and #2, respectively. The illustrations of the model are shown in Fig. 1.

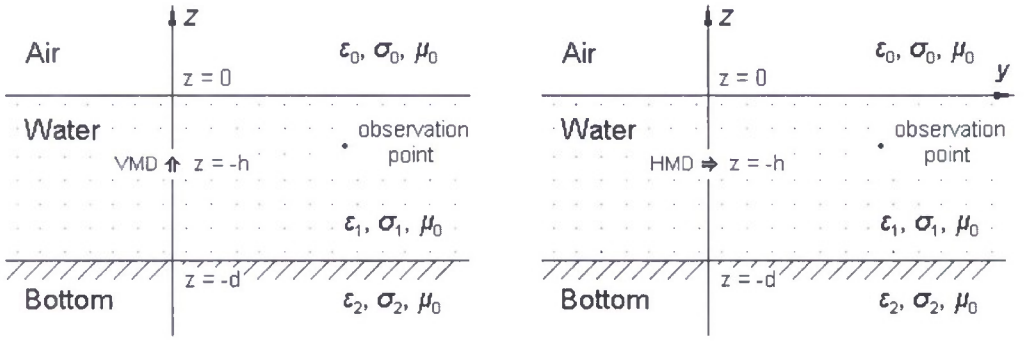

Vertical magnetic dipole Horizontal magnetic dipole

Fig. 1 Model illustrations

As marked in the figure, ε_i (i = 0, 1 and 2) is the permittivity, μ_i is the permeability and σ_i is the conductivity of the i^{th} layer. $\varepsilon_i = \varepsilon_{ri}\varepsilon_0$, where ε_{ri} is the relative permittivity and ε_0 is the permittivity of free space. For non-magnetic media, $\mu_1 = \mu_2 = \mu_0$.

An integral form of the electric vector potential is used to derive the solutions to the fields. For VMD and HMD cases the vector potentials can be respectively written as (assuming the time variation is $e^{j\omega t}$)

VMD	$F_z^0 = k_1 \int_0^\infty f_1(\lambda) \cdot e^{-u_0 z} \lambda J_0(\lambda\rho) d\lambda \qquad (z \geq 0)$ $F_z^1 = k_1 \frac{e^{\gamma_1 R}}{R} + k_1 \int_0^\infty [f_2(\lambda) \cdot e^{-u_1 z} + f_3(\lambda) \cdot e^{u_1 z}] \cdot \lambda J_0(\lambda\rho) d\lambda \qquad (-d \leq z \leq 0)$ $F_z^2 = k_1 \int_0^\infty f_4(\lambda) \cdot e^{u_2 z} \lambda J_0(\lambda\rho) d\lambda \qquad (z \leq -d)$
HMD	$F_y^0 = k_1 \int_0^\infty f_1(\lambda) e^{-u_0 z} \lambda J_0(\lambda\rho) d\lambda \qquad (z \geq 0)$ $F_y^1 = k_1 \frac{e^{\gamma_1 R}}{R} + k_1 \int_0^\infty \left[f_2(\lambda) e^{-u_1 z} + f_3(\lambda) e^{u_1 z} \right] \lambda J_0(\lambda\rho) d\lambda \qquad (-d \leq z \leq 0)$

HMD (*contd.*)	$F_y^2 = k_1 \int_0^\infty f_4(\lambda) e^{u_2 z} \lambda J_0(\lambda\rho) d\lambda \qquad (z \leq -d)$ $F_z^0 = k_1 \frac{\partial}{\partial y} \int_0^\infty g_1(\lambda) e^{-u_0 z} \lambda J_0(\lambda\rho) d\lambda \qquad (z \geq 0)$ $F_z^1 = k_1 \frac{\partial}{\partial y} \int_0^\infty \left[g_2(\lambda) e^{-u_1 z} + g_3(\lambda) e^{u_1 z} \right] \lambda J_0(\lambda\rho) d\lambda \qquad (-d \leq z \leq 0)$ $F_z^2 = k_1 \frac{\partial}{\partial y} \int_0^\infty g_4(\lambda) e^{u_2 z} \lambda J_0(\lambda\rho) d\lambda \qquad (z \leq -d)$

In these expressions of the vector potentials, the constants k_1 and γ_i and the variable u_i are defined as (i = 0, 1 and 2):

$$k_1 = \frac{j\omega\mu\varepsilon_1' IdA}{4\pi}$$

$$\gamma_i^2 = -\omega^2 \mu \varepsilon_i'$$

$$u_i = \sqrt{(\lambda^2 + \gamma_i^2)}$$

where $\varepsilon_i' = \varepsilon_i - j\frac{\sigma_i}{\omega}$ is the complex permittivity of the i^{th} layer, $\mathrm{Re}(\gamma_i) < 0$ and $\mathrm{Re}(u_i) > 0$. The term $k_1 \frac{e^{\gamma_1 R}}{R}$ in F_z^1 for VMD and F_y^1 for HMD represents the radiation field by the dipole in an infinite homogeneous medium (infinite lake water for this case). It can be written in integral form as

$$k_1 \frac{e^{\gamma_1 R}}{R} = \begin{cases} k_1 \int_0^\infty u_1^{-1} e^{-u_1(z+h)} \lambda J_0(\lambda\rho) d\lambda & (z+h) \geq 0 \\ k_1 \int_0^\infty u_1^{-1} e^{u_1(z+h)} \lambda J_0(\lambda\rho) d\lambda & (z+h) \leq 0 \end{cases}$$

where $R = (x^2 + y^2)^{1/2}$.

The coefficient functions f_1 through f_4 and g_1 through g_4 can be determined from the tangential components of the electric and magnetic fields E and H, respectively, at the interfaces (z = 0 and z = -d planes), They are

VMD

$$f_1(\lambda) = -2\left(\frac{\varepsilon_0'}{\varepsilon_1'}\right)\cdot\left[\frac{(u_1+u_2)e^{-u_1(h-d)}+(u_1-u_2)e^{u_1(h-d)}}{(u_0-u_1)(u_2-u_1)e^{-u_1 d}-(u_0+u_1)(u_2+u_1)e^{u_1 d}}\right];$$

$$f_2(\lambda) = \left(\frac{u_1-u_2}{u_1}\right)\cdot\frac{e^{-u_1 d}\left[(u_0-u_1)e^{-u_1 h}-(u_0+u_1)e^{u_1 h}\right]}{(u_0-u_1)(u_2-u_1)e^{-u_1 d}-(u_0+u_1)(u_2+u_1)e^{u_1 d}};$$

$$f_3(\lambda) = \left(\frac{u_0-u_1}{u_1}\right)\cdot\left[\frac{(u_1-u_2)e^{u_1(h-d)}+(u_1+u_2)e^{-u_1(h-d)}}{(u_0-u_1)(u_2-u_1)e^{-u_1 d}-(u_0+u_1)(u_2+u_1)e^{u_1 d}}\right];$$

$$f_4(\lambda) = 2\left(\frac{\varepsilon_2'}{\varepsilon_1'}\right)\cdot\frac{e^{u_2 d}\left[(u_0-u_1)e^{-u_1 h}-(u_0+u_1)e^{u_1 h}\right]}{(u_0-u_1)(u_2-u_1)e^{-u_1 d}-(u_0+u_1)(u_2+u_1)e^{u_1 d}}.$$

HMD

$$f_1 = \frac{2\varepsilon_0'}{DEN}\left[(\varepsilon_1'u_2-\varepsilon_2'u_1)e^{u_1(h-d)}-(\varepsilon_1'u_2+\varepsilon_2'u_1)e^{-u_1(h-d)}\right];$$

$$f_2 = \frac{1}{u_1}\frac{(\varepsilon_1'u_0-\varepsilon_0'u_1)(\varepsilon_2'u_1-\varepsilon_1'u_2)e^{-u_1(h+d)}+(\varepsilon_1'u_0+\varepsilon_0'u_1)(\varepsilon_1'u_2-\varepsilon_2'u_1)e^{u_1(h-d)}}{DEN};$$

$$f_3 = \frac{1}{u_1}\frac{(\varepsilon_0'u_1-\varepsilon_1'u_0)(\varepsilon_1'u_2-\varepsilon_2'u_1)e^{u_1(h-d)}+(\varepsilon_1'u_0-\varepsilon_0'u_1)(\varepsilon_1'u_2+\varepsilon_2'u_1)e^{-u_1(h-d)}}{DEN};$$

$$f_4 = \frac{2\varepsilon_2'e^{u_2 d}}{DEN}\left[(\varepsilon_1'u_0-\varepsilon_0'u_1)e^{-u_1 h}-(\varepsilon_0'u_1+\varepsilon_1'u_0)e^{u_1 h}\right]$$

where $DEN = (\varepsilon_0'u_1-\varepsilon_1'u_0)(\varepsilon_2'u_1-\varepsilon_1'u_2)e^{-u_1 d}-(\varepsilon_0'u_1+\varepsilon_1'u_0)(\varepsilon_1'u_2+\varepsilon_2'u_1)e^{u_1 d}$.

$$g_1 = \frac{\varepsilon_2'(\varepsilon_1'-\varepsilon_0')\left[(u_2-u_1)e^{-u_1 d}-(u_1+u_2)e^{u_1 d}\right]f_1+2\varepsilon_0'u_1(\varepsilon_1'-\varepsilon_2')e^{-u_2 d}f_4}{\varepsilon_1'\varepsilon_2'\cdot DEN_1};$$

$$g_2 = \frac{\varepsilon_2'(\varepsilon_1'-\varepsilon_0')(u_2-u_1)e^{-u_1 d}f_1+\varepsilon_0'(\varepsilon_1'-\varepsilon_2')(u_0+u_1)e^{-u_2 d}f_4}{\varepsilon_0'\varepsilon_2'\cdot DEN_1};$$

$$g_3 = \frac{\varepsilon_2'(\varepsilon_0'-\varepsilon_1')(u_1+u_2)e^{u_1 d}f_1+\varepsilon_0'(\varepsilon_2'-\varepsilon_1')(u_0-u_1)e^{-u_2 d}f_4}{\varepsilon_0'\varepsilon_2'\cdot DEN_1};$$

$$g_4 = \frac{2\varepsilon_2'u_1(\varepsilon_0'-\varepsilon_1')e^{u_2 d}f_1+\varepsilon_0'(\varepsilon_1'-\varepsilon_2')\left[(u_0+u_1)e^{u_1 d}-(u_0-u_1)e^{-u_1 d}\right]f_4}{\varepsilon_0'\varepsilon_1'\cdot DEN_1}$$

where $DEN_1 = (u_0-u_1)(u_2-u_1)e^{-u_1 d}-(u_0+u_1)(u_1+u_2)e^{u_1 d}$.

With these coefficient functions being determined, the analytical solutions to the E and H fields can be derived from Maxwell's equations. The complete expressions for E and H fields in the water layer are listed below.

VMD: E and H fields in water (Medium #1):

$$E_{\phi}^{1} = \frac{1}{\varepsilon_1'}\frac{\partial F_z^1}{\partial \rho}$$

$$= \frac{k_1}{\varepsilon_1'}\left[\begin{cases} \int_0^{\infty} -\lambda^2 u_1^{-1} e^{-u_1(z+h)} J_1(\lambda\rho)d\lambda & (z+h \geq 0) \\ \int_0^{\infty} -\lambda^2 u_1^{-1} e^{u_1(z+h)} J_1(\lambda\rho)d\lambda & (z+h \leq 0) \end{cases} - \int_0^{\infty}\left[e^{-u_1 z} f_2 + e^{u_1 z} f_3\right]\lambda^2 J_1(\lambda\rho)d\lambda\right]$$

$$H_{\rho}^{1} = -\frac{j}{\omega\mu\varepsilon_1'}\frac{\partial^2 F_z^1}{\partial\rho\partial z}$$

$$= \frac{IdA}{4\pi}\left[\begin{cases} \int_0^{\infty} \lambda^2 e^{-u_1(z+h)} J_1(\lambda\rho)d\lambda & (z+h \geq 0) \\ \int_0^{\infty} -\lambda^2 e^{u_1(z+h)} J_1(\lambda\rho)d\lambda & (z+h \leq 0) \end{cases} + \int_0^{\infty}\left[e^{-u_1 z} f_2 - e^{u_1 z} f_3\right]\lambda^2 u_1 J_1(\lambda\rho)d\lambda\right]$$

$$H_{z}^{1} = -\frac{j}{\omega\mu\varepsilon_1'}\left(\frac{\partial^2}{\partial z^2} + \gamma_1^2\right)F_z^1$$

$$= \frac{IdA}{4\pi}\left[\begin{cases} \int_0^{\infty} \lambda^3 u_1^{-1} e^{-u_1(z+h)} J_0(\lambda\rho)d\lambda & (z+h \geq 0) \\ \int_0^{\infty} \lambda^3 u_1^{-1} e^{u_1(z+h)} J_0(\lambda\rho)d\lambda & (z+h \leq 0) \end{cases} + \int_0^{\infty}\left[e^{-u_1 z} f_2 + e^{u_1 z} f_3\right]\lambda^3 J_0(\lambda\rho)d\lambda\right]$$

HMD: E and H fields in water (Medium #1):

$$E_{x}^{1} = -\frac{1}{\varepsilon_1'}\left(\frac{\partial F_z^1}{\partial y} - \frac{\partial F_y^1}{\partial z}\right)$$

$$= \frac{k_1}{\varepsilon_1'}\left\{\begin{cases} \int_0^{\infty} -\lambda e^{-u_1(z+h)} J_0(\lambda\rho)d\lambda & (z+h \geq 0) \\ \int_0^{\infty} \lambda e^{u_1(z+h)} J_0(\lambda\rho)d\lambda & (z+h \leq 0) \end{cases} + \int_0^{\infty}\left[-e^{-u_1 z} f_2 + e^{u_1 z} f_3\right]u_1\lambda J_0(\lambda\rho)d\lambda\right.$$

$$\left. + \int_0^{\infty}\left(e^{-u_1 z} g_2 + e^{u_1 z} g_3\right)\left[\lambda J_0(\lambda\rho)\sin^2(\phi) + \frac{1}{\rho}J_1(\lambda\rho)\cos(2\phi)\right]\lambda^2 d\lambda\right\}$$

$$E_{y}^{1} = \frac{1}{\varepsilon_1'}\frac{\partial F_z^1}{\partial x}$$

$$= -\frac{k_1}{\varepsilon_1'}\int_0^{\infty}\left(e^{-u_1 z} g_2 + e^{u_1 z} g_3\right)\left[\lambda J_0(\lambda\rho) - \frac{2}{\rho}J_1(\lambda\rho)\right]\lambda^2 \sin(\phi)\cos(\phi)d\lambda$$

$$E_z^1 = -\frac{1}{\varepsilon_1'}\frac{\partial F_y^1}{\partial x}$$
$$= \frac{k_1}{\varepsilon_1'}\int_0^\infty \left(\begin{cases} u_1^{-1}e^{-u_1(z+h)} & (z+h \geq 0) \\ u_1^{-1}e^{u_1(z+h)} & (z+h \leq 0) \end{cases} + e^{-u_1 z} f_2 + e^{u_1 z} f_3 \right) \lambda^2 J_1(\lambda\rho)\cos(\phi) d\lambda$$

$$H_x^1 = -\frac{j}{\omega\mu\varepsilon_1'}\frac{\partial}{\partial x}\left(\frac{\partial F_y^1}{\partial y} + \frac{\partial F_z^1}{\partial z}\right)$$
$$= -\frac{IdA}{4\pi}\int_0^\infty \left(\begin{cases} u_1^{-1}e^{-u_1(z+h)} & (z+h \geq 0) \\ u_1^{-1}e^{u_1(z+h)} & (z+h \leq 0) \end{cases} + e^{-u_1 z} f_2 + e^{u_1 z} f_3 - u_1 e^{-u_1 z} g_2 + u_1 e^{u_1 z} g_3 \right)$$
$$\cdot \left[\lambda J_0(\lambda\rho) - \frac{2}{\rho} J_1(\lambda\rho) \right] \lambda^2 \sin(\phi)\cos(\phi) d\lambda$$

$$H_y^1 = -\frac{j}{\omega\mu\varepsilon_1'}\left[\frac{\partial}{\partial y}\left(\frac{\partial F_y^1}{\partial y} + \frac{\partial F_z^1}{\partial z}\right) - \gamma_1^2 F_y^1\right]$$
$$= -\frac{IdA}{4\pi}\int_0^\infty \left(\begin{cases} u_1^{-1}e^{-u_1(z+h)} & (z+h \geq 0) \\ u_1^{-1}e^{u_1(z+h)} & (z+h \leq 0) \end{cases} + e^{-u_1 z} f_2 + e^{u_1 z} f_3 - u_1 e^{-u_1 z} g_2 + u_1 e^{u_1 z} g_3 \right)$$
$$\cdot \left[\lambda J_0(\lambda\rho)\sin^2(\phi) + \frac{1}{\rho} J_1(\lambda\rho)\cos(2\phi) \right] \lambda^2 d\lambda$$
$$+ \int_0^\infty \left(\begin{cases} u_1^{-1}e^{-u_1(z+h)} & (z+h \geq 0) \\ u_1^{-1}e^{u_1(z+h)} & (z+h \leq 0) \end{cases} + e^{-u_1 z} f_2 + e^{u_1 z} f_3 \right) \cdot \gamma_1^2 \lambda J_0(\lambda\rho) d\lambda$$

$$H_z^1 = -\frac{j}{\omega\mu\varepsilon_1'}\left[\frac{\partial}{\partial z}\left(\frac{\partial F_y^1}{\partial y} + \frac{\partial F_z^1}{\partial z}\right) - \gamma_1^2 F_z^1\right]$$
$$= -\frac{IdA}{4\pi}\int_0^\infty \left(\begin{cases} -e^{-u_1(z+h)} & (z+h \geq 0) \\ e^{u_1(z+h)} & (z+h \leq 0) \end{cases} - u_1 e^{-u_1 z} f_2 + u_1 e^{u_1 z} f_3 + \lambda^2 e^{-u_1 z} g_2 + \lambda^2 e^{u_1 z} g_3 \right)$$
$$\cdot \lambda^2 J_1(\lambda\rho)\sin(\phi) d\lambda$$

$$\phi = \text{atan}(x/y)$$

With the analytical solutions, the electric and magnetic fields in the water layer can be easily calculated. Fig. 2 through Fig. 5 show some examples of the field calculation. The parameters used are listed in the table below.

	Air	Water	Bottom
Relative permittivity, ε_{ri} ($\varepsilon_i = \varepsilon_0 \varepsilon_{ri}$)	1	1	1
Conductivity, σ (S/m)	0	0.018	0.012
Permeability, μ (H/m)	$4\pi\times10^{-7}$	$4\pi\times10^{-7}$	$4\pi\times10^{-7}$
d (m)	300		
h (m)	can vary from 0 to 300		
Dipole moment IdA ($A\cdot m^2$)	2500		
frequency f (Hz)	1000		

Since H_z and H_y are respectively the dominant components for VMD and HMD cases, the results for only these two components are plotted here. Fig. 2 and Fig.3 give the magnitude of H_z for the VMD case. Given the measurement equipment available, the minimum detectable magnetic field is also indicated in the figure (dotted line). From experimental data, $|H|_{min} = 4\times10^{-5}$ A/m and $|E|_{min} = 1\times10^{-6}$ V/m.

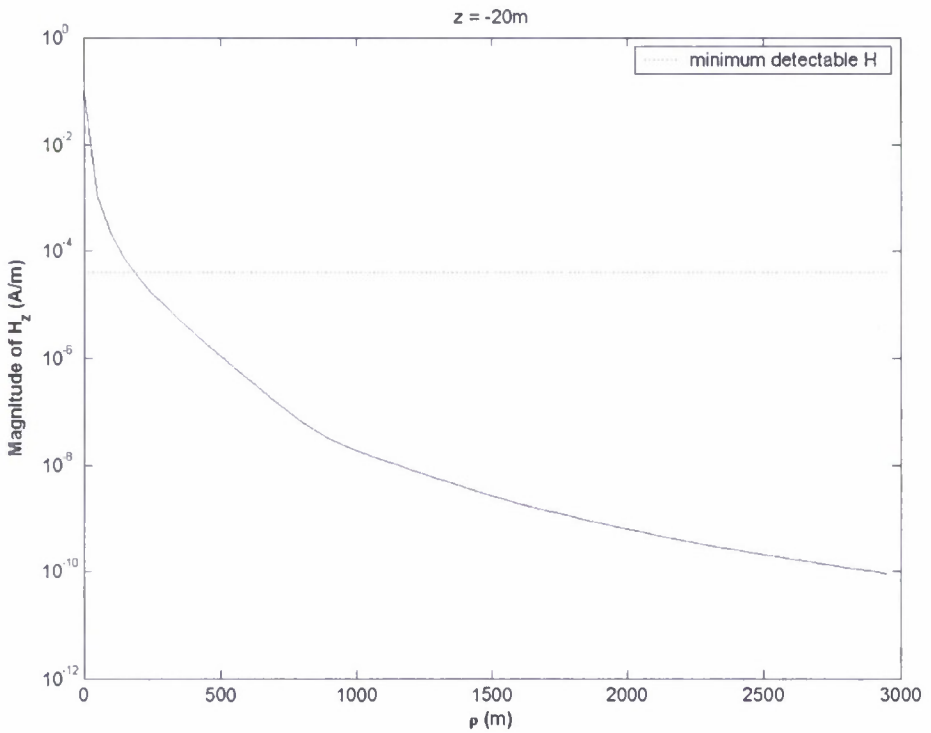

Fig. 2 Magnitude of H_z in water for VMD case: VMD is 5m below surface (h = 5m), observation points horizontally placed at z = -20m

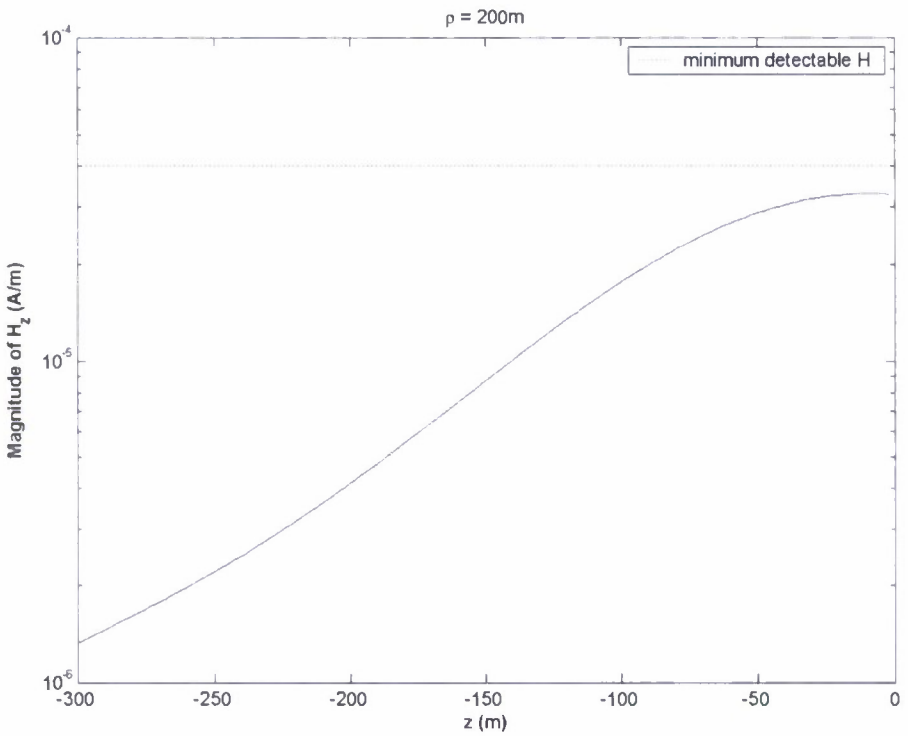

Fig. 3 Magnitude of H_z in water for VMD ease: VMD is 5m below surfaee (h = 5m), observation points vertically placed at ρ = 200m

Fig. 4 and Fig. 5 give the magnitude of H_y for the HMD case:

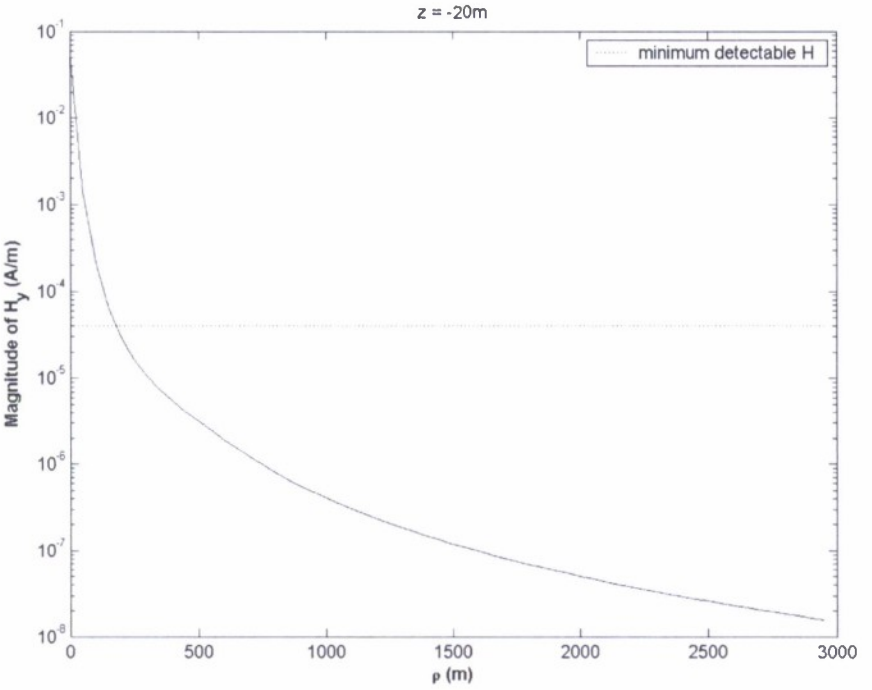

Fig. 4 Magnitude of H_y in water for HMD ease: HMD is 5m below surfaee (h = 5m), observation points horizontally placed at z = -20m, $\Phi = \pi/3$

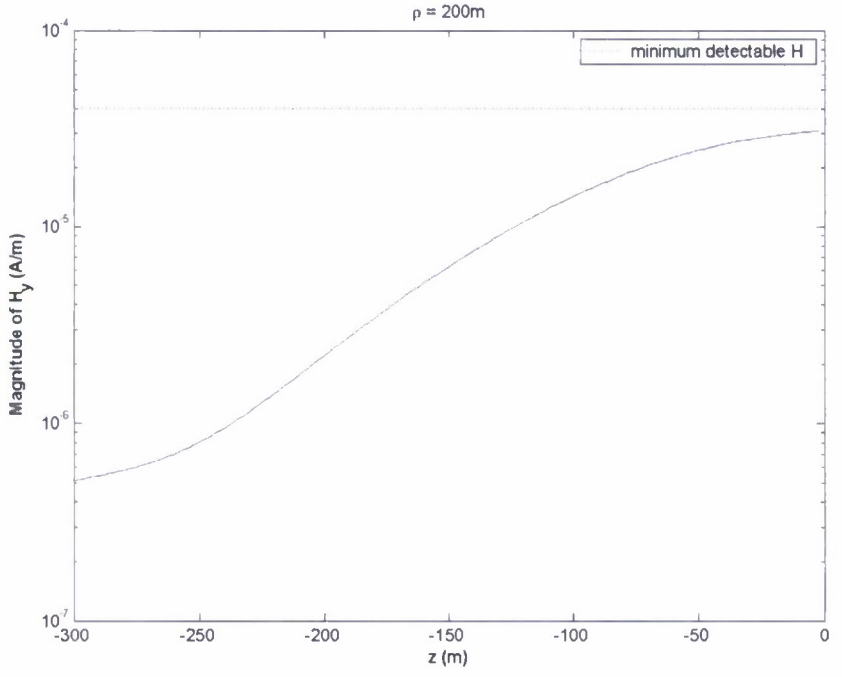

Fig. 5 Magnitude of H_y in water for HMD ease: HMD is 5m below surface (h = 5m), observation points vertically placed at ρ = 200m, $\Phi = \pi/3$

Validation

After the analytical solutions were developed, several tests were conducted to validate the results.

VMD Case:

First, the formulas for the field were checked against to the results obtained in some references. Reference [1] provides formulas for the calculation of magnetic fields inside a semi-infinite conducting medium. If let $\varepsilon_2 = \varepsilon_1$ and $\sigma_2 = \sigma_1$, our 3-layer model reduces to a 2-layer model, which is analogous to the model used in [1]. Then our equations of the coefficient functions reduce to equation (11) and (12) in [1]. A MATLAB program was written to numerically compute our field formulas. Again, if the model is reduced to a 2-layer (air-water) model, our simulation result matches with Fig. 2 in [1].

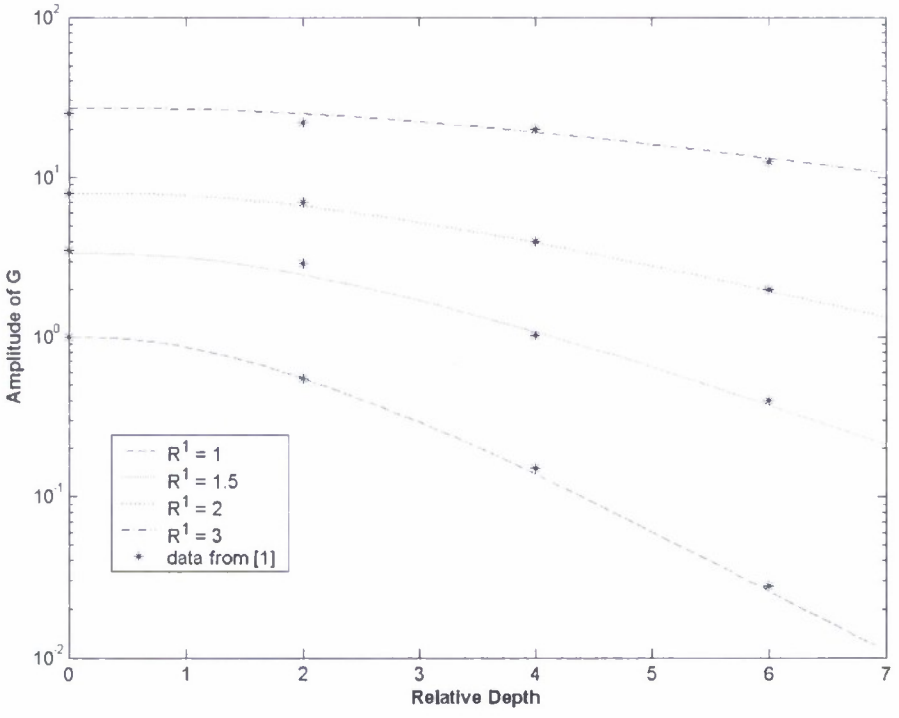

Fig. 6 Comparing our numerical simulation results with Fig. 2 in [1]

To facilitate comparison, a factor G is introduced that is proportional to H_z, which is also used in [1]:

$$H_z = \frac{IdA}{2\pi(z+h)^3} G$$

Likewise, R^1 is a ratio defined as

$$R^1 = \frac{z+h}{|z-h|}$$

where z is the depth of the observation point and h is the depth of the dipole source. If let $\varepsilon_0 = \varepsilon_1$ and $\sigma_0 = \sigma_1$, the 3-layer model reduces to a 2-layer (water-bottom) model. The same simulation results for the factor G were obtained as shown in Fig. 2 of [1] when the dipole source was put at the water-bottom interface.

Second, the results reported here were also compared to those for a homogeneous-medium case. For instance, if the VMD source is placed in the middle of the second layer, where it is far away from both interfaces, our field results are very close to that of a quasi-static case in which a dipole radiates in the infinite homogeneous medium. Figure 7 shows an example for this. For the 3-layer case, the dipole is 150m away from both of the interfaces. The calculation of field perfectly matches with that for the quasi-static case.

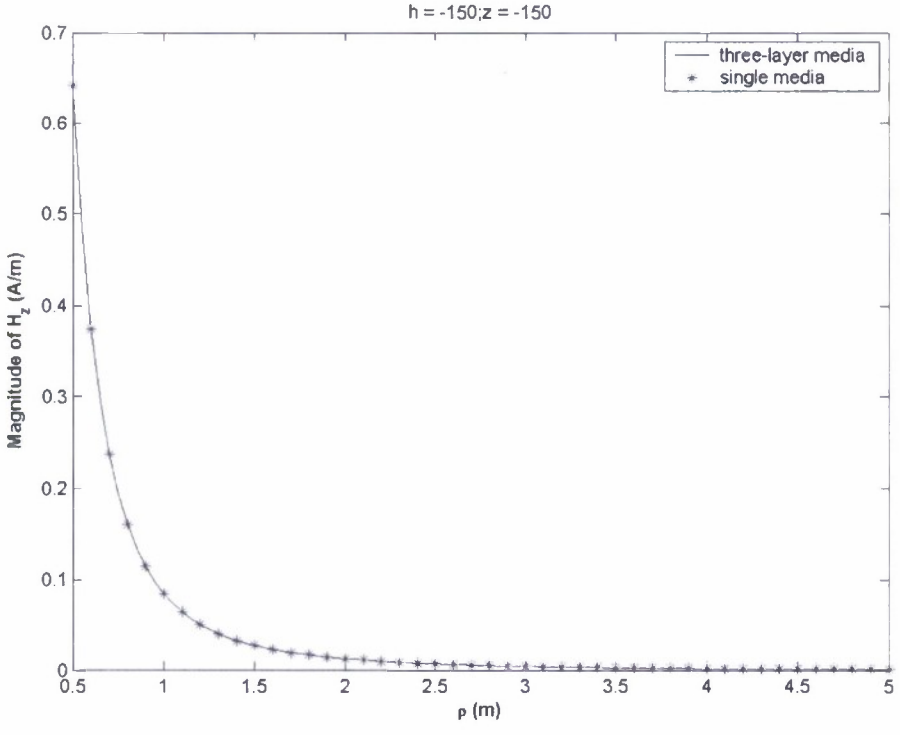

Fig. 7 VMD simulation result compared to homogeneous case

Third, the boundary conditions across both the air-water and water-bottom interfaces were checked. It is not difficult to find the solutions to the fields in the first and third layer of the medium using the same method described in part 1. Figures 8a and 8b show the boundary conditions data at the air-water interface for the VMD case.

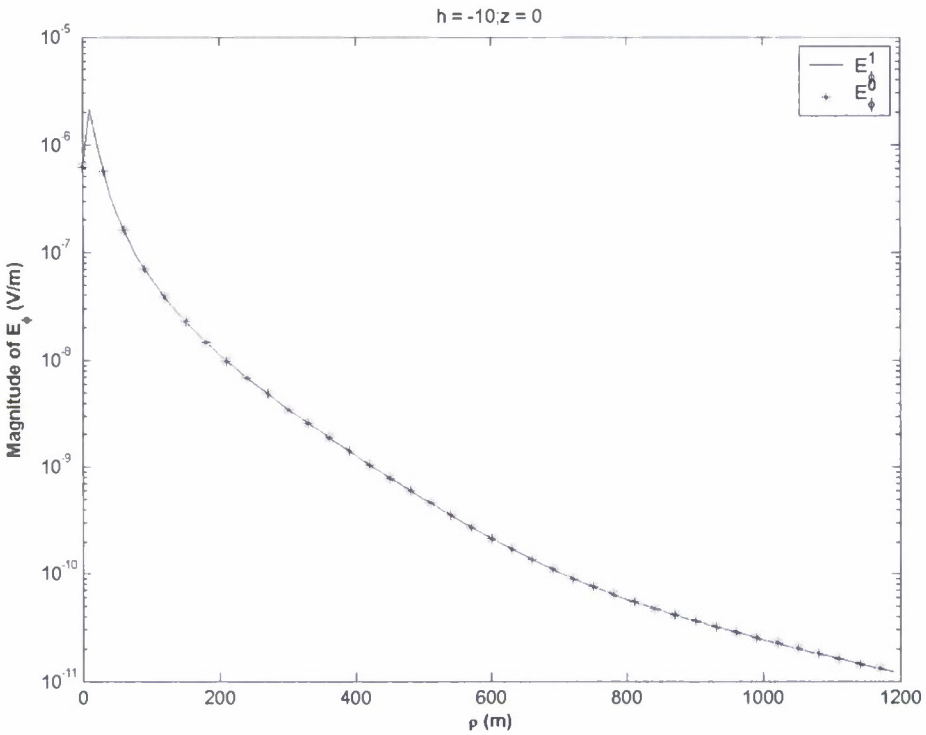

(a) E_{Φ}

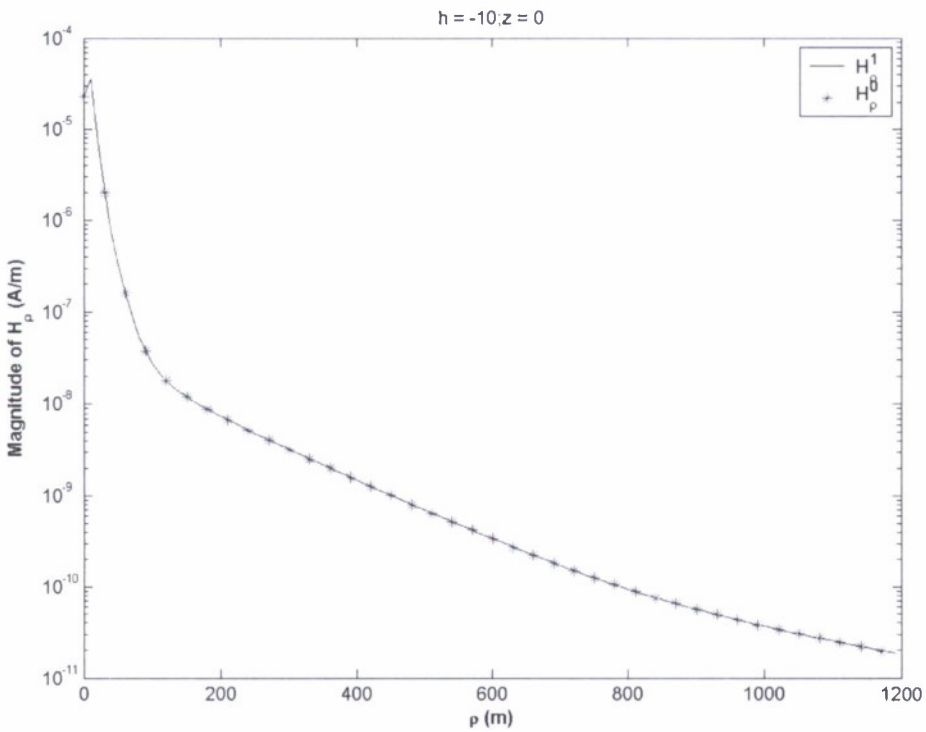

(b) H_{ρ}

Fig. 8 Checking tangential E & H fields along the air-water interface for VMD case

The continuity of tangential fields along the water-bottom interface was also validated. The results are not be plotted here.

HMD Case:

For HMD case, the same strategies as in VMD case were used to validate the results. First, when the model was reduced to the 2-layer case, our equations for the coefficient functions reduced to equations (21) through (23) in [2]. Then the simulations shown in Fig. 2 in [2] were repeated. Our numerical simulations (for fields in line with dipole, refer to Fig. 2 in [2]) of the factor A are plotted in Fig. 9.

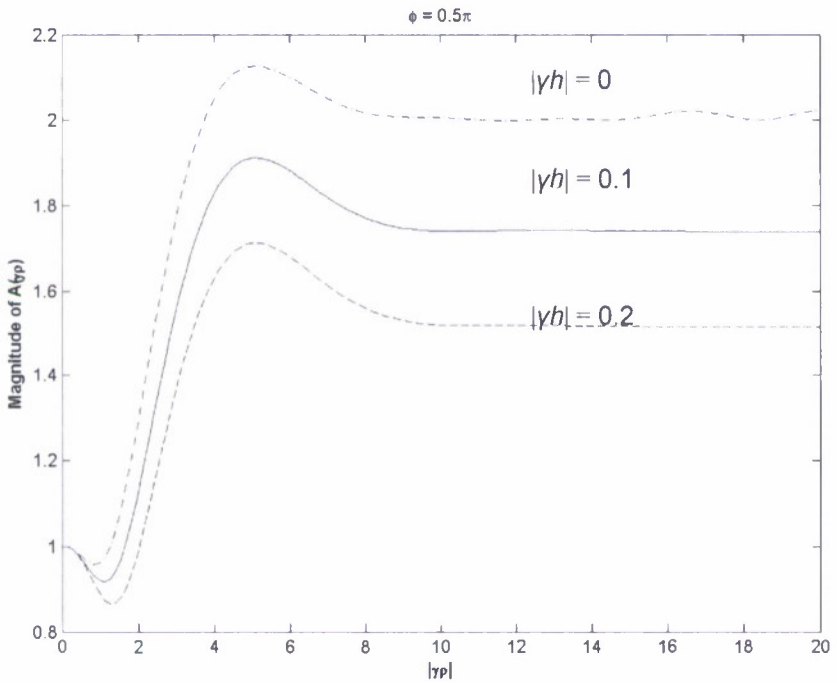

Fig. 9 Magnitude of factor A (proportional to H_y) vs relative horizontal distance (Φ=0.5π)

The factor A is proportional to the H_y field. In [2], it is defined as

$$A(\gamma h) = \frac{2\pi\rho^3}{IdA} H_y$$

It should be mentioned that our results are not exactly the same as those given in [2]. The starting points and the final values match. But there is an overshoot in Fig. 9, which cannot be seen in Fig. 2 of [2]. The reason for this appears to be that in [2] a first order approximation of integral was used to calculate the field, while our simulation used the analytical solution, which can give more accurate calculation. To verify that ours is correct, the boundary conditions for this specific case were also checked. From our numerical data, the factor A (which is proportional to tangential H) is perfectly continuous across the interface, as shown in Fig. 10. This provides supporting evidence to that our data are more accurate than that in [2]. The tangential E fields across the interface were also checked and the similar results are shown in Fig. 10.

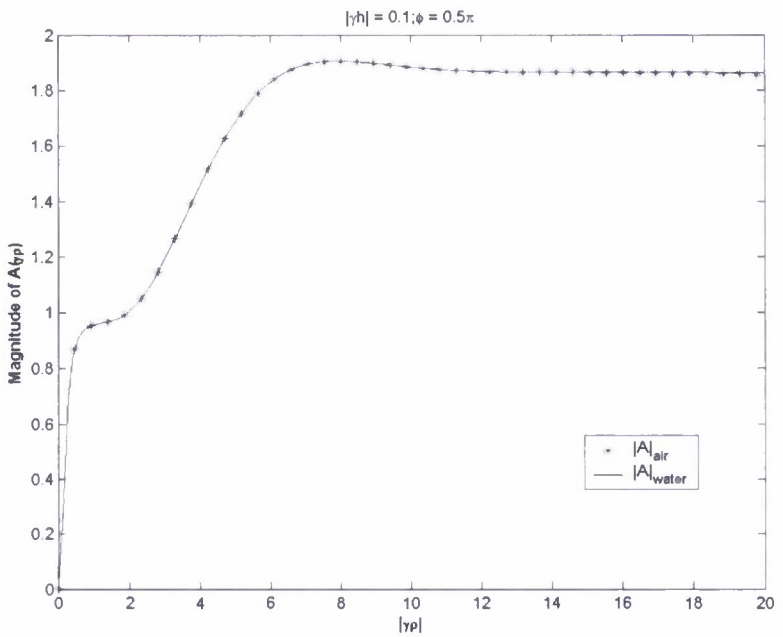

(a) $|\gamma h|=0.1$

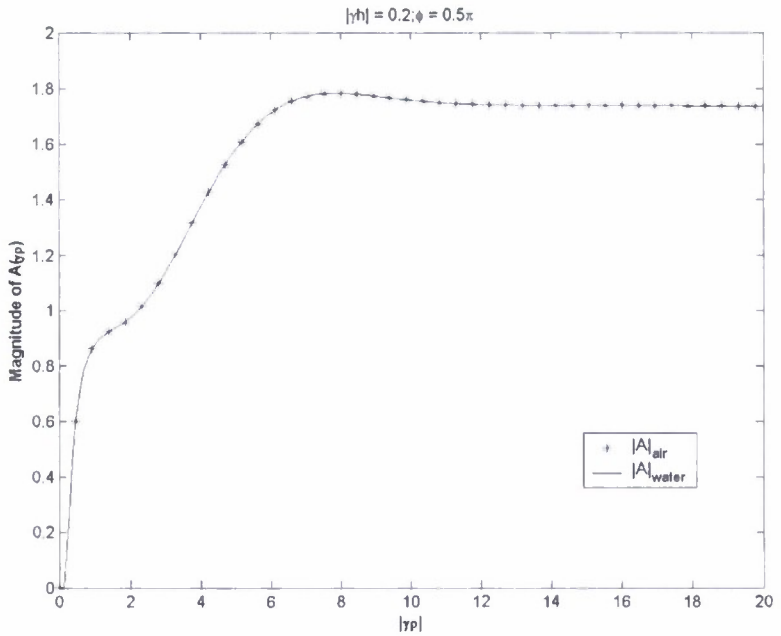

(b) $|\gamma h|=0.2$

Fig. 10: Boundary conditions associated with factor A ($\Phi=0.5\pi$)

The results of HMD were also compared to those for the quasi-static case. They also match with each other very well.

Finally, the boundary conditions were checked for both tangential electric and magnetic fields across air-water and water-bottom interfaces. The results for the electric field at the water-bottom interface are shown in Fig. 11.

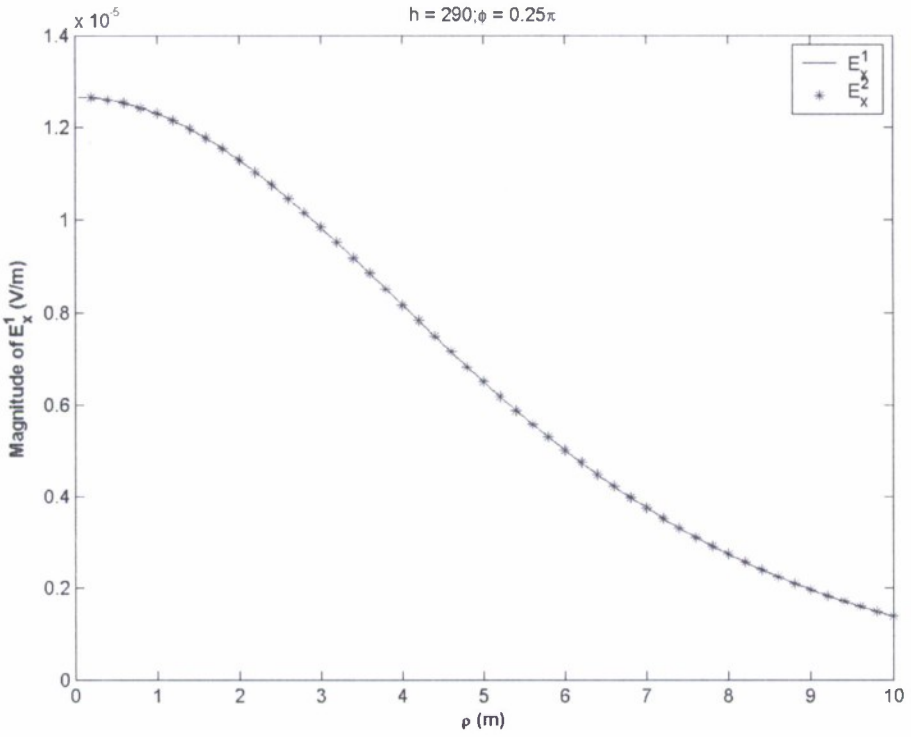

(a) E_x

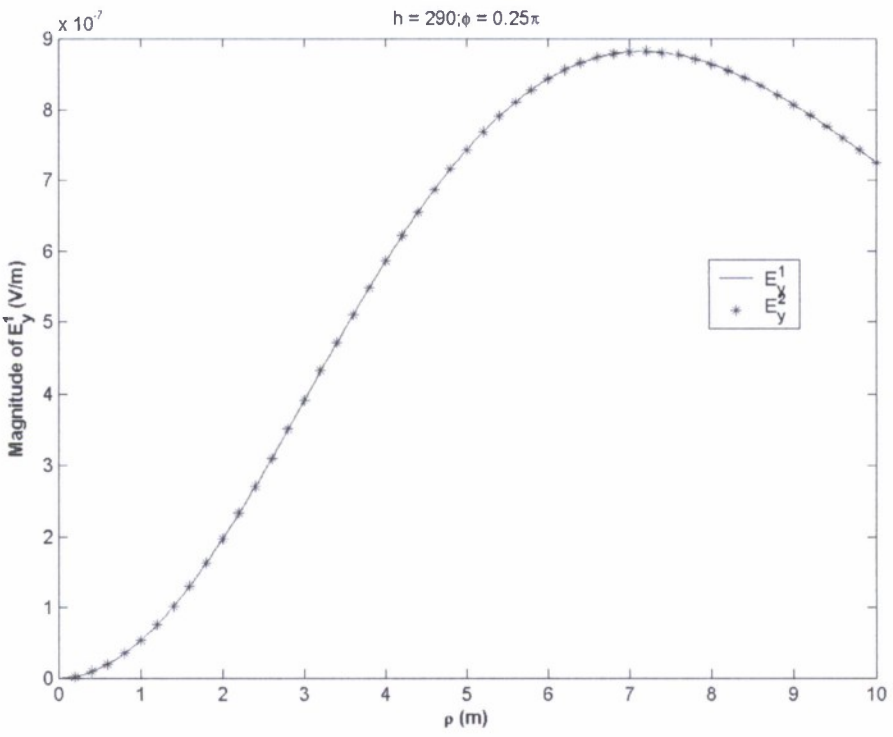

(b) E_y

Fig. 11: Tangential E fields along the water-bottom interface for HMD case

References

[1] A.K. Sinha and P.K. Bhattacharya, "Vertical Magnetic Dipole Buried Inside a Homogeneous Earth", Radio Science, Vol. 1 (New series), No. 3, pp 379-395, 1966.
[2] J.R. Wait and L.L. Campbell, "The Fields of An Oscillating Magnetic Dipole Immersed In a Semi-infinite Conducting Medium", Journal of Geophysical Research, Vol. 58, No. 2, pp167-178, 1953.

Appendix B: FDTD Method

Dennis Sullivan

Department of Electrical and Computer Engineering, University of Idaho

Abstract

The major effort of the FDTD group for the past year has been to extend the range of FDTD simulations underwater without using enormous computer resources. It has included the development of a near-field, far-field formulation to allow the use of large cells in simulating the far field, and the development of an interpolation scheme to improve accuracy when large cells are used in the far field. It has also included the development of a new perfectly matched layer to reduce the size of the surrounding computational domain. A reformulation of the basic FDTD method has been introduced to improve stability during extremely long computation times.

Introduction

In the past year, the FDTD simulation group has accomplished the following:

1. The reformulation of the FDTD code for greater stability at low frequencies.

2. The development of a near-field/far-field formulation that allows the simulation of energy sources in the near field with relatively small cells, while the far field is simulated with larger cells to extend the range of the simulation.

3. The development of a perfectly matched layer (PML) for simulations in lossy media at ELF frequencies.

4. The preliminary investigation of a high-resolution interpolation method to improve resolution in the far field.

Accomplishments:

Details of the above accomplishments are given in the following sections.

1. Reformulation of the FDTD for greater stability at low frequencies.

The formulation of the Maxwell's equations that is normally used in FDTD

simulations is [1]

$$\varepsilon_0 \frac{\partial \boldsymbol{D}}{\partial t} = \nabla \times \boldsymbol{H} \tag{1.1 a}$$

$$\boldsymbol{D}(\omega) = \varepsilon^*(\omega)\boldsymbol{E}(\omega) \tag{1.1 b}$$

$$\mu_0 \frac{\partial \boldsymbol{H}}{\partial t} = -\nabla \times \boldsymbol{E}. \tag{1.1 c}$$

This formulation allow a great deal of flexibility in simulating complicated materials because the various materials are specified by the complex dielectric constant $\varepsilon^*(\omega)$ and having a separate equation to calculate the electric field E from the flux density D allows one to bring to bear signal processing techniques for the formulation in FDTD. The simulation of a lossy material leads to equations of the form

$$E_z^n = \frac{D_z^n - S^n}{\varepsilon_r + \dfrac{\Delta t \cdot \sigma}{\varepsilon_0}}, \tag{1.2 a}$$

$$S^n = S^{n-1} + E_z^n. \tag{1.2 b}$$

This formulation is very stable at radio frequencies and above, but leads to potential instabilities at ELF frequencies. The reason is Eq. (1.2 b), which is the time domain implementation of an integration. An ELF FDTD simulation is over a fraction of a wavelength, which means that an integration like Eq. (1.2b) is constantly increasing. Over long simulations on the order of 20,000 iterations, this has occasionally led to instability.

Alternatively, we begin with the following time-domain Maxwell's equations

$$\varepsilon_r \varepsilon_0 \frac{\partial \boldsymbol{E}}{\partial t} = \nabla \times \boldsymbol{H} - \sigma \boldsymbol{E} \tag{1.3 a}$$

$$\mu_0 \frac{\partial \boldsymbol{H}}{\partial t} = -\nabla \times \boldsymbol{E}. \tag{1.3 b}$$

We assume the cell size is Δx and the time step is Δt. The E_x^{n+1} can now be calculated from [2, 3]

$$E_x^{n+1}(k) = ca(k)E_x^n(k) + cb(k)\left[H_y^{n+1/2}(k+1/2) - H_y^{n+1/2}(k-1/2)\right], \tag{1.4 a}$$

where

$$ca = \left(1 + \frac{\Delta t \cdot \sigma}{\varepsilon_r \varepsilon_0}\right)^{-1}, \quad cb = ca\frac{\Delta t}{(\varepsilon_r \varepsilon_0 \Delta x)}. \tag{1.4 b}$$

There is a crucial choice that was made here. Usually, the E_x term next to the

conductivity is averaged across the two time steps

$$\varepsilon_r \frac{E_x^{n+1}(k) - E_x^n(k)}{\Delta t} + \left(\frac{\sigma}{\varepsilon_0}\right)\left(\frac{E_x^{n+1}(k) + E_x^n(k)}{2}\right) = \frac{1}{\varepsilon_0}\frac{H_y^{n+1/2}(k+1/2) - H_y^{n+1/2}(k-1/2)}{\Delta x},$$

which would lead to the following expression for *ca*:

$$ca = \left(1 - \frac{\Delta t \cdot \sigma}{2\varepsilon_r \varepsilon_0}\right) / \left(1 + \frac{\Delta t \cdot \sigma}{2\varepsilon_r \varepsilon_0}\right). \tag{1.5}$$

At ELF frequencies in lossy media, the *ca* of Eq. (1.5) would be negative, leading to a potentially unstable condition. (The implementation of Eq. (1.3 b) into FDTD is straight-forward and will not be presented here.)

There is another choice that leads to substantially larger time steps, and therefore, substantially faster solutions. Once the cell size Δx is chosen, the time step must be chosen to satisfy the Courant condition, which in three dimensions is

$$\Delta t \le \frac{\Delta x}{\sqrt{3} \cdot c_{\max}}, \tag{1.6}$$

where $c_{\max}$ is usually the speed of light in a vacuum. The complex dielectric constant is calculated by

$$\varepsilon_r^* = \varepsilon_r + \frac{\sigma}{j\omega\varepsilon_0}.$$

The materials of interest for this project and their dielectric properties are listed in Table one. At ELF frequencies, the imaginary part of the dielectric constant will dominate the magnitude for all the materials except air. Therefore, increasing the dielectric constants of mud or metal to 80 would make very little difference. If we assume every material in Table one has a real dielectric constant of 80, then $c_{\max} = c_0 / \sqrt{80}$ and the time step is almost an order of magnitude greater. (c_0 is the speed of light in a vacuum.) Even though air is one of the materials used in the simulations, air is a boundary medium in this project. It presents almost perfect reflection to an electromagnetic signal in water, even if the higher dielectric constant is used.

Table 1. The properties of the materials used in the simulations described in this paper [4].

Material	ε_r	$\sigma\ (S/m)$
Air	1	0
Lake water	80	0.018
Mud	40	0.002
Metal	1	10^7

2. The development of a near-field/far-field formulation

By utilizing the equivalence principle [5], a method has been developed to model the radiating sources with a relatively high resolution, and to model the far field with larger cells to extend the potential problem space. Two, three-dimensional FDTD problem spaces are utilized to implement the near-to-far field transformation (Fig. 2.1) [6, 7]. A problem space with a relatively small cells size (1 m^3) is used to model the source (Fig. 2.1a). Another problem space with larger cells (13 m^3) is used to model the far field (Fig. 2.1b). The ratio of 13 to 1 between far and near field cells size is somewhat arbitrary. For the simulations in this paper, it resulted in near and far field problem spaces of about the same size. Each problem space is surrounded by a perfectly matched layer. (A new PML for ELF frequencies and lossy media has been developed and is discussed in section 3.) Each problem space contains a three-dimensional transfer surface where the equivalence principle is implemented. The tangential fields calculated on the transfer surface in the near field are impressed on the transfer surface in the far field to form the far field source. This is illustrated in Fig. 2.2.

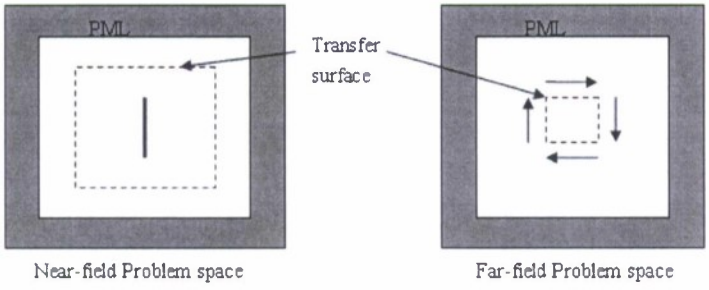

Figure 2.1. Two problem spaces are used in the FDTD simulation.

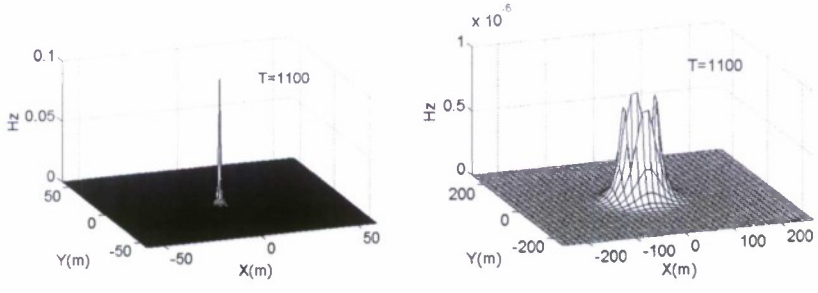

(a) (b)

Figure 2.2. (a) Near-field mesh plot, (b) Far-field mesh plot.

Validation

In this section, the results of the near to far field transformation are compared to analytic results calculated using Sommerfeld's half-space (SHS) problem. Sommerfeld's half space problem calculates the resulting fields from an oscillating dipole near a plane interface separating two homogeneous half-space regions, as illustrated in Fig. 2.3. This method was well described in Appendix A and in the literature [8] and will not be repeated here. In Fig. 2.3, the upper layer is air, the middle layer is water and the lower level is mud. The water layer in the middle is 300 meters thick. The monitor lines represent the places where comparisons between the methods will be made.

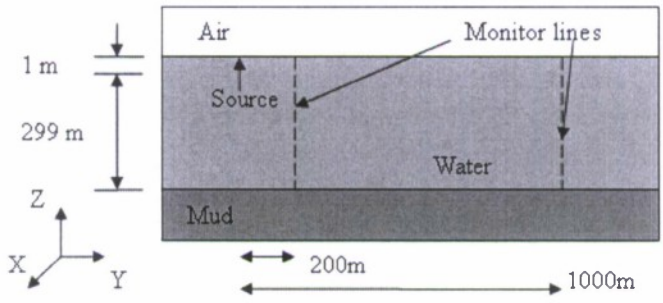

Figure 2.3. Diagram of the comparison between the FDTD near-to-far field transformation and the SHS method. The source is 1 meter below the air-water interface.

Comparisons at 200 meters and 1000 meters are shown in Fig. 2.4a and Fig. 2.4b, respectively. The amplitudes in each figure are calculated by the method of two-equations, two-unknowns [3]. The horizontal coordinate is the distance to the air/water surface and the vertical coordinate is the magnitude of the field. The discrete symbols represent the FDTD calculations and the different kinds of lines represent the calculations by SHS method. Clearly, the results of the comparisons are very good in all cases.

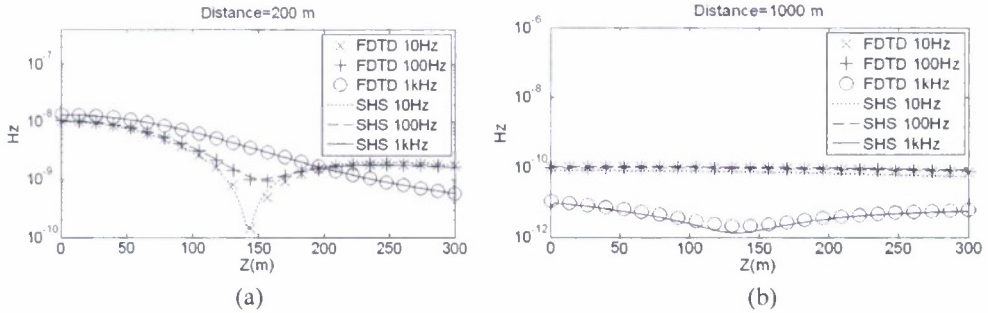

(a) (b)

Figure 2.4. Comparisons of the FDTD simulations and the SHS calculations for the cell size ratio of 10. The source is near the upper surface of the water layer. (a) 200 meter case, (b) 1000 meter case.

This section illustrates the use of FDTD with a near field, far field transformation in simulating a more realistic case. One of the goals of the simulation is to verify the accuracy of the modeling with measured data that will be made in a lake. Because the lake bed is not flat, analytical approaches cannot be used to solve the problem.

The antennas that will be used in the transmission are four meter by four meter rectangular current loops. Figure 2.5a illustrates how this is simulated in the XY plane in the FDTD space. Metal can be simulated by insuring that an E field is zero at a particular point in the space. Therefore, using cells that are one meter cubed, the metal loop antenna is simulated at the corresponding E_x or E_y positions, as shown in Fig. 5a. Since the radius of the wire of the antennas is considerably less than the 1 meter cells size, the thin rod approximation [9] is used to model the wire at these positions.

In FDTD, a current cannot be simulated directly, but it can be simulated indirectly by using Ampere's circuit Law [5] and specifying the surrounding H fields:

$$I = \oint \frac{1}{\mu_0} \mathbf{H} \cdot d\mathbf{l} . \tag{2.1}$$

By impressing a hard source on one of the E_y fields, a value is induced on the surrounding H fields, as shown in Fig. 2.5b. This results in a current, via Eq. (2.1).

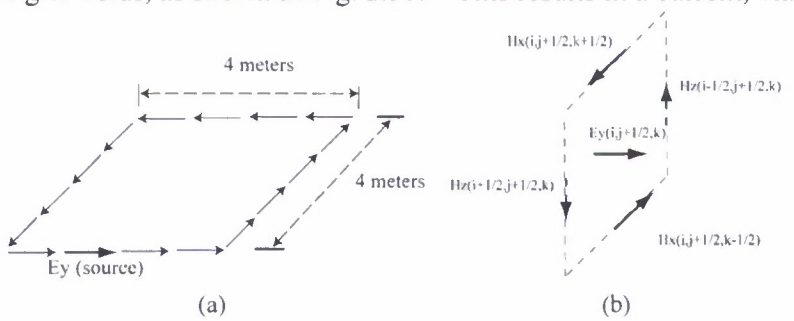

Figure 2.5. The simulation of a four meter by four meter current loop in FDTD.

A model of the lake bed is created for the far field domain (Fig. 2.6). The cells are ten meters cubed. The shape of the lower surface of the water layer shows a complex geometry structure similar to a real lake bed.

Figure 2.7 shows the results of the near to far field simulation using the current loop source in the near field and the lake bed in the far field. Results are given for two different places, 200 meters and 1000 meters from the source, and at three different frequencies, 10, 100, and 1000 Hz. These simulations were done on an HP DL140

GE Quad Core and required about 6 hours. Both the near and far field problem spaces were 120 cells cubed.

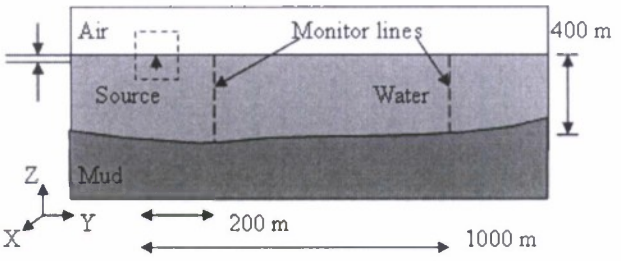

Figure 2.6. The lake bed that is simulated in the far field. The cells are 10 meters cubed. The source is the current loop located one meter below the surface.

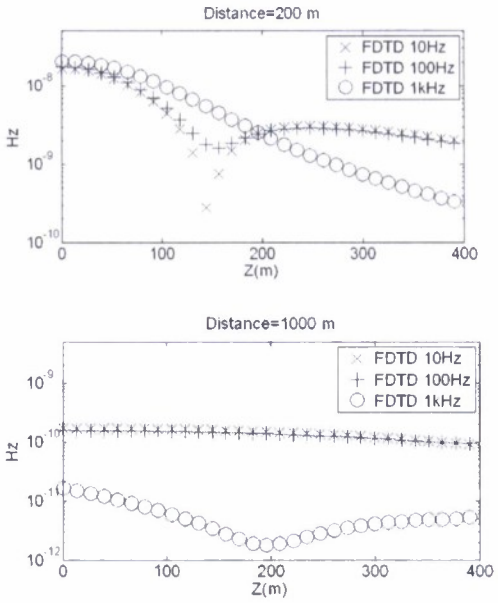

(a) The results at 200 meters (b) The results at 1000 meters.

Figure 2.7. Results of the simulation illustrated in Fig. 2.6.

3. The development of a perfectly matched layer (PML) for lossy media at ELF frequencies

Berenger [10] assumed that any plane wave propagating in the direction d near the PML could be broken up into the part traveling perpendicular to the PML, $d_{\perp}$, and the part traveling parallel, $d_{\parallel}$ (Fig. 3.1). The two conditions for the PML are

1. It must have the same impedance as free space and not present a loss to the wave traveling parallel to the interface [Eq. (3.1)].

2. It must increase the artificial electric and magnetic conductivities such that the impedance still matches that of the free space.

Both of these conditions are met by increasing the electric and magnetic conductivities in the PML such that

$$\eta = \sqrt{\frac{\mu_0}{\varepsilon_0}} = \sqrt{\frac{\mu_0\left(1+\dfrac{\sigma_H}{j\omega\mu_0}\right)}{\varepsilon_0\left(1+\dfrac{\sigma_E}{j\omega\varepsilon_0}\right)}}. \tag{3.1}$$

Note that this impedance is a real number.

Berenger implemented Eq. (3.1) into the FDTD formulation by a split-step formulation that broke each electric and magnetic field up into two components. Most applications assume that the background medium in the main problem space is free space.

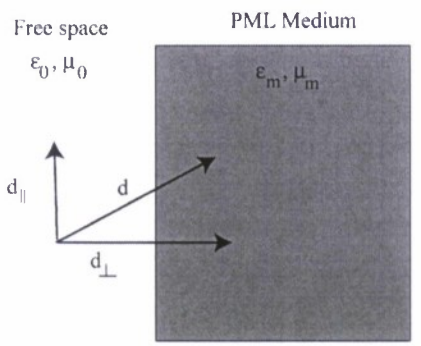

Figure 3.1. The PML is implemented by assuming any propagating wave can be broken up into a part that is perpendicular to the PML interface and a part that is parallel to it.

The PML in a lossy medium at ELF frequencies

When the background medium is lake water and the frequencies are in the ELF region, the situation is different [10, 11]. Lake water has a dielectric constant of 80 and a conductivity of 0.018 S/m. For lake water at 1 kHz, the complex dielectric constant is

$$\varepsilon_w^* = \varepsilon_w + \frac{\sigma_w}{j\omega\varepsilon_0} = 80 + \frac{0.018}{j\left(2\pi\times10^3\right)\left(8.85\times10^{-12}\right)}$$
$$= 80 - j3.24\times10^5 \cong -j3.24\times10^5.$$

Therefore, the impedance is

$$\eta_w = \sqrt{\frac{\mu_0}{\dfrac{\sigma_w}{j\omega\varepsilon_0}}}. \tag{3.2}$$

This impedance can be written in polar coordinates as

$$\eta_w = |\eta_w| \angle 45^o .$$

Notice that because the loss term dominates, the impedance is 45 degrees in phase. The impedance of the PML material must remain at this value, but at the same time increase the loss further as it goes perpendicular into the PML. This can be accomplished by adding a factor s to the conductivity and the permeability

$$\eta_m = \sqrt{\frac{s \cdot \mu_0}{\frac{s \cdot \sigma_w}{j\omega\varepsilon_0}}} . \tag{3.3}$$

This causes the PML medium to absorb outgoing waves faster than the water medium, but also avoids reflections from the PML medium.

Implementation into FDTD

We begin by looking at the implementation of E_x and H_z propagating in the y direction perpendicular to the PML:

$$\varepsilon_w \varepsilon_0 \frac{\partial E_{xy}}{\partial t} + \sigma_w E_{xy} = \frac{\partial H_z}{\partial y},$$

$$\mu_0 \frac{\partial H_z}{\partial t} = \frac{\partial E_{xy}}{\partial y} .$$

Note that $\varepsilon_w = 80$ and $\sigma = 0.018$ for water. The first step to convert the equation to the FDTD formulation is to approximate all partial derivatives as difference equations. The spatial derivatives are not as important in this discussion, so we write

$$\frac{\partial H_z}{\partial y} \cong \frac{del\_H}{\Delta x} .$$

Taking the usual finite-difference approximation to the time derivatives gives

$$\varepsilon_w \frac{E_{xy}^{n+1} - E_{xy}^{n}}{\Delta t} + \left(\frac{\sigma_w}{\varepsilon_0}\right) E_{xy}^{n+1} = \frac{1}{\varepsilon_0} \frac{del\_H}{\Delta x},$$

and solving for the updated version of E_{xy}^{n+1}

$$E_{xy}^{n+1} - E_{xy}^{n} + \left(\frac{\Delta t \cdot \sigma_w}{\varepsilon_w \varepsilon_0}\right) E_{xy}^{n+1} = \frac{\Delta t}{\varepsilon_w \varepsilon_0} \frac{del\_H}{\Delta x} .$$

From this we can develop the FDTD equations:

$$E_{xy}^{n+1} = ca \cdot E_{xy}^{n} + cb \cdot del\_H , \tag{3.4 a}$$

$$ca = \frac{1}{\left(1 + \frac{\Delta t \cdot \sigma_w}{\varepsilon_w \varepsilon_0}\right)} \quad cb = \frac{\Delta t / (\varepsilon_w \varepsilon_0 \Delta x)}{\left(1 + \frac{\Delta t \cdot \sigma_w}{\varepsilon_w \varepsilon_0}\right)} del\_H \cdot \tag{3.4 b}$$

A similar procedure for the H field gives

$$H_z^{n+1/2} = H_z^{n-1/2} + db \cdot del\_E, \tag{3.5 a}$$

where

$$db = \frac{\Delta t}{\mu_0 \cdot \Delta x}. \tag{3.5 b}$$

Recall that to implement the PML we increase the conductivity and the permeability at the same rate by a constant parameter s as shown in Eq. (3.3). This is easy to do for the permeability. We add another parameter fy to Eq. (5 a)

$$H_z^{n+1/2} = H_z^{n-1/2} + fy(j) \cdot db \cdot del\_E. \tag{3.6}$$

Instead of changing db to $\Delta t/(2 \cdot \mu_0 \cdot \Delta x)$, for instance, we simply set $fy(j) = 0.5$.

However, increasing σ_w is not so straight-forward. Notice that it involves both ca and cb. Rather that recalculate the parameters for each increase, we define another parameter

$$gy(j) = \frac{\left(1 + \frac{\Delta t \cdot \sigma_w}{\varepsilon_w \varepsilon_0}\right)}{\left(1 + \frac{\Delta t \cdot s \cdot \sigma_w}{\varepsilon_w \varepsilon_0}\right)} \tag{3.7}$$

The factor is added to Eq. (3.4 a):

$$E_{xy}^{n+1} = gy(j) \cdot ca \cdot E_{xy}^n + gy(j) \cdot cb \cdot del\_H. \tag{3.8}$$

Note that it is necessary to split the E fields, but not the H fields.

Results

In this section we illustrate the effectiveness of the lossy medium PML. We will start with the problem space illustrated in Fig. 3.2a, which is 80 cells cubed. Each cell is 25 meters cubed. The source is a single-cell electric dipole. After 4000 time steps, the amplitude is calculated along a monitor line as shown in Fig. (3.2 b).

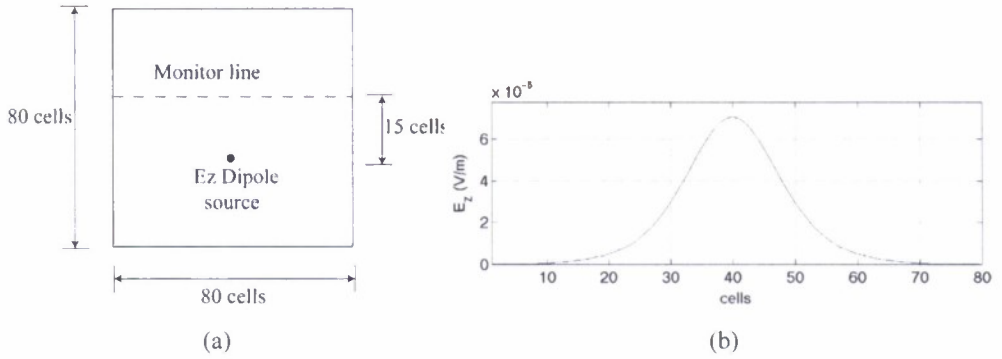

Figure 3.2. (a) A dipole source is located in the 80^3 problem space. Once steady state has been reached, the amplitude is determined at a transverse line 15 cells from the source. The cells are 25 m^3. (b) The amplitude at the monitor line after 4000 time steps.

The simulation is then repeated for the truncated problem space shown in Fig. 3a where a four-cell PML has been added. In this simulation the right wall has been moved in to within ten cells of the source. The results are plotted in Fig. 3b along with the results of the previous simulation. For comparison, Fig. 3c is the same simulation with no PML on the truncated wall.

In one final simulation, the problem space is reduced to 60 x 20 x 20 cells, as illustrated in Fig. 3.4a. The results are shown in Fig. 3.4b where the results of the original simulation of Fig. 2 are presented for comparison. The amplitudes on the monitor line within five cells of the center are identical. If these values represent the information of interest, then the addition of the PML means a problem space of 60 x 20 x 20 = 24,000 cells instead of the original 80^3 = 510,000 cells. Fig. 3.5c repeats the simulation with no PML on the boundaries.

Because this PML was developed for lossy media, it is not particularly effective in free space or other lossless media. Most of the simulations for this project include the water surface and therefore, free space is part of the problem. What remains to be developed is an interface mechanism so the lossy PML can be used underwater and the normal PML used above water.

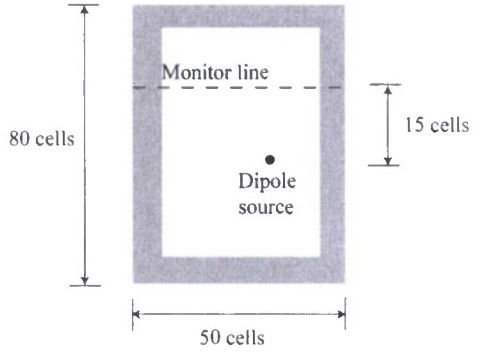

(a)

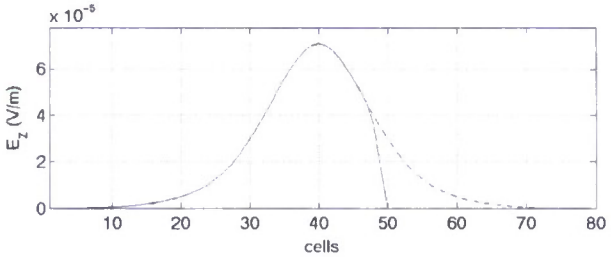

(b)

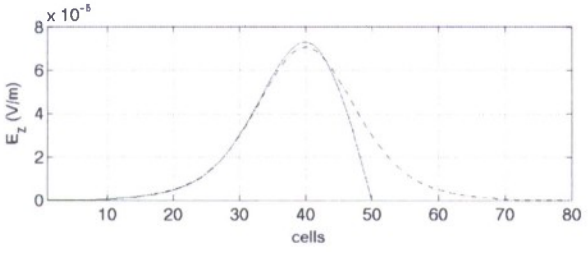

(c)

Figure 3.3. (a) The problem spaee is truncated to ten cells to the lcft of the source. A four-cell lossy PML has been added to each boundary. (b) The solid line is the amplitude for the simulation in (a), while the dashed line is from the 80 eell monitor line of Fig. 3.2. (c) The same simulation with no PML.

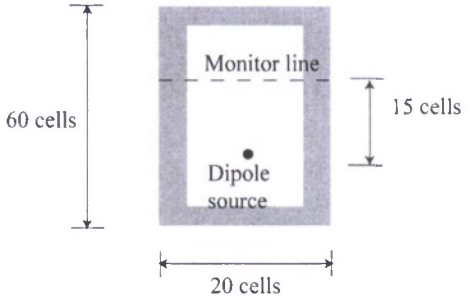

(a)

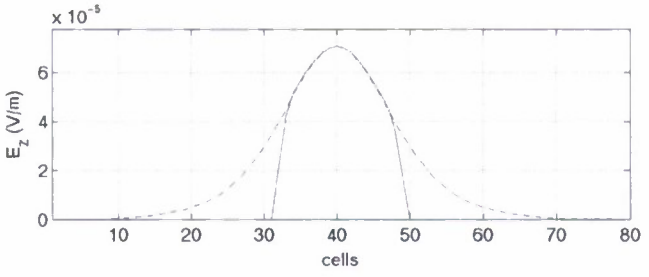

(b)

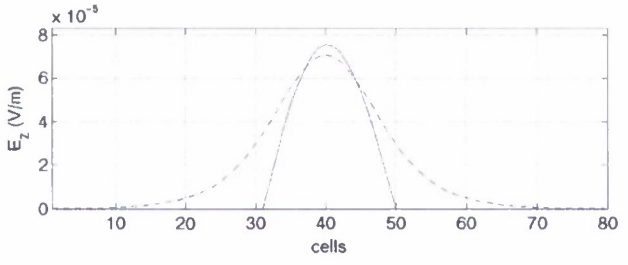

(c)

Figure 3.4. (a) A simulation similar to Fig. (3.2) but with the problem space truncated to 60 x 20 x 20 cells. (b) The solid line is the amplitude for the smaller problem space while the dashed line is the larger problem space of Fig. 3.2. (c) The same comparison when a 60 x 20 x20 problem space with no PML is used.

4. The development of a high resolution interpolation method

Section 2 described the near-field, far-field transformation that enables us to use relatively large cells to extend the computational domain. However, there may be times when relatively high resolution is needed in the far field. Figure 4.1 illustrates such a possibility where an indentation in the sea floor would be lost if cells on the order of 10 meters cubed are used.

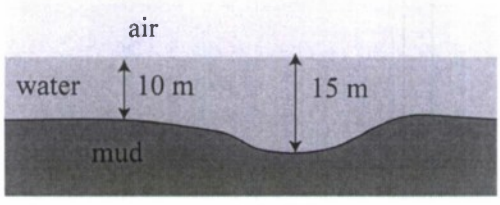

Figure 4.1. Typical contours in shallow water. Cell sizes on the order of ten meters cubed are used in the far field. This could result in substantial errors when modeling shallow water where mines are often planted.

One solution is a correction to the FDTD fields that is made after the core FDTD

simulation is finished [13]. In the following discussion $\boldsymbol{E}$ will represent the true electric field around a boundary, and $\tilde{\boldsymbol{E}}$ represent the averaged FDTD electric field value (Fig. 4.2). At an arbitrary boundary, the electric fields can be represented as the sum of the tangential and normal components

$$\boldsymbol{E} = \boldsymbol{E}_t + \boldsymbol{E}_n \tag{4.1}$$

$$\tilde{\boldsymbol{E}} = \tilde{\boldsymbol{E}}_t + \tilde{\boldsymbol{E}}_n \tag{4.2}$$

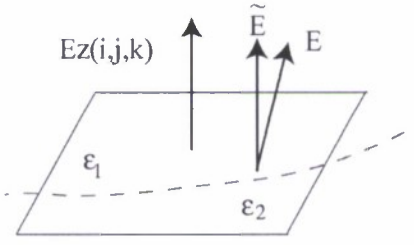

Figure 4.2. FDTD only calculates values at discrete points, such as $E_z(i,j,k)$. Values at other positions can be approximated by interpolating

Two assumptions are made: The tangential components of the true and the FDTD values are equal

$$\boldsymbol{E}_t = \tilde{\boldsymbol{E}}_t, \tag{4.3}$$

and the normal flux densities are equal

$$\boldsymbol{D}_n = \tilde{\boldsymbol{D}}_n. \tag{4.4}$$

Equation (4.4) leads to the following relationship between the E fields:

$$\varepsilon \boldsymbol{E}_n = \tilde{\varepsilon}\tilde{\boldsymbol{E}}_n, \tag{4.5}$$

where ε is the true dielectric constant at that point and $\tilde{\varepsilon}$ is the averaged dielectric constant usually used in the FDTD formulation. From Eq. (4.3) and (4.5), it can be shown that the true electric field can be calculated by the averaged FDTD E field with a correction term added. Specifically, in the z direction the E field is

$$E_z = \tilde{E}_z + \left(\frac{\tilde{\varepsilon}_z}{\varepsilon_z} - 1\right)\tilde{E}_{zn} \tag{4.6}$$

where $\tilde{E}_{zn}$ is calculated by

$$\tilde{E}_{zn} = \hat{n}_z \cdot \left[\left(\hat{\boldsymbol{n}} \cdot \tilde{\boldsymbol{E}}\right)\hat{\boldsymbol{n}}\right]. \tag{4.7}$$

In Eq. (4.7) $\hat{\boldsymbol{n}}$ is the gradient of the dielectric constant and $\hat{n}_z$ is the z component of

$\hat{n}$. The correction is applied after the FDTD simulation is finished. A more detailed explanation is in [14].

Verification of the Method

In order to verify the accuracy of the interpolation scheme described in the previous section, we used an analytic method based on Legendre polynomials [4]. This method calculates the values of the electric field inside a layered sphere in an electric field. Table one is a list of the materials of interest, along with their dielectric properties. In particular, we will look at the values on an axis at forty-five degrees in the YZ plane because it is at these slanted angles that the largest FDTD error occurs.

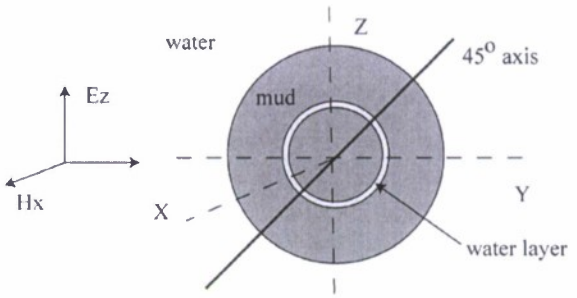

Figure 4.3. A layered sphere is used to provide an analytie eheek to the FDTD data. The background medium is water; the sphere is half mud, half water. The narrow layer in the middle is either mud or water.

We show the results for an FDTD simulation using 10 m cubed cells at 1 kHz in a water medium both before and after the correction is applied. The sphere in Fig. 4.3 has the characteristics of mud. The thin layer is ¼ a cell wide and has the characteristics of water. Figure 4.4 displays the results. FDTD alone sees the basic features but tends to average the magnitudes out. After the interpolation, a much better agreement is attained, even though the layer is less that one cell.

Since the interpolation takes place only after the FDTD simulation, it adds nothing to the computation time and very little to the needed computer resources. This approach provides more accuracy when large cells on the order of ten meters are used for long range, underwater FDTD simulation.

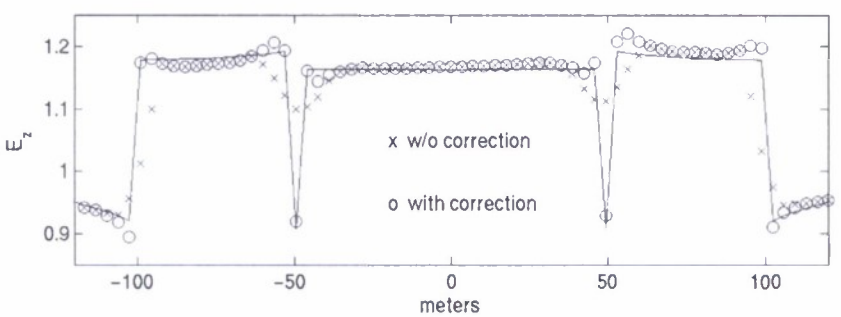

Figure 4.4. Results for a 1/4 cell (2.5 m) layer of water. The straight line is the analytic values, the x's are from and FDTD simulation before the correction, and the o's are the values after the correction.

Conclusion

The effort over the past year has concentrated on maximizing the effectiveness of the FDTD simulation over long distances. Towards this end, a more stable formulation of the FDTD algorithm was introduced to insure stability during very long simulations. A near-field, far-field transformation was implemented to allow radiating sources to be simulating with relatively small cells to maintain accuracy, while the far field is simulated with larger cells to increase he simulation distance. A perfectly matched layer was developed to work more effectively for highly lossy materials at ELF frequencies. This decreases the need for a large surrounding computational space. Finally, a correction to the FDTD method has been implemented that allows the determination of the fields at a higher resolution than the FDTD cells.

One of the tasks that remain is the merging of the new underwater PML with the old PML for free space. The underwater PML is not effective in free space. While the propagation of ELF signals in free space is not a major interest for this project, it could play a substantial role in maintaining accuracy of the underwater simulations.

References

1. D. M. Sullivan, *Electromagnetic Simulation Using the FDTD Method.* New York, NY: IEEE Press, 2000
2. D. M. Sullivan and Y. Xia, "Underwater FDTD simulation at low frequencies," IEEE International Symposium on Antennas and Propagation, San Diego, CA, July 5-12, 2008.
3. Y. Xia and D. M. Sullivan, "Underwater FDTD simulation at extremely low frequencies," *IEEE Antennas and Propagations Wireless Letters,* Vol. 7, pp.661-664, 2008.
4. D. K. Chen, *Field and Wave Electromagnetics,* 2nd Ed., New York: Addison-Wesley, 1989.
5. Roger Harrington, *Time-Harmonic Electromagnetic Fields,* New York, NY: McGraw-Hill, 1961.
6. Y. Xia and D. M. Sullivan, "Near to far field transformation for underwater ELF simulation," IEEE International Symposium on Antennas and Propagation, San Diego, CA, July 5-12, 2008.
7. Y. Xia, D. M. Sullivan, Z. Li, and R. Olsen "Long distance underwater ELF simulation using a near-to-far field transformation", *IEEE Antennas and Propagations Wireless Letters*, scheduled for publication, 2009.
8. J. R. Wait, *Electromagnetic Wave Theory,* Harper and Row, New York, NY, 1985

9. J. Nadobny, R. Pontalti, D. M. Sullivan, W. Wladarczk, A. Vaccari, P. Deuflhard, and P. Wust, "A thin-rod approximation for the improved modeling of bare and insulated cylindrical antennas using the FDTD method," *IEEE Trans. Ant. Prop.*, vol. 51, pp. 1780-1796, Aug. 2003
10. J. P. Berenger, "A perfectly matched layer for the absorption of electromagnetic waves," *J. Comp. Physics,* Vol. 114, pp.185-200, 1994.
11. D. M. Sullivan and Y. Xia, "A perfectly matched layer for lossy media at extremely low frequencies, *IEEE Antennas and Propagations Wireless Letters*, submitted for review.
12. D. M. Sullivan and Y. Xia, "A perfectly matched layer for lossy media at extremely low frequencies, to be presented at the IEEE International Symposium on Antennas and Propagation, Charleston, SC, June 1-5, 2009.
13. J. Nadobny, D. M. Sullivan, P. Wust, M. Seebass, P. Deuflhard, and R. Felix, "A high-resolution interpolation at arbitrary interfaces fro the FDTD method," *IEEE Trans. Anten. Prop.,* Vol. 46, pp. 1759-1766, Nov. 1998.
14. Y. Xia, A. Mansouri, D. M. Sullivan, and J.Nadobny, "High resolution interpolation for underwater FDTD simulation at ELF frequencies," to be presented at the IEEE International Symposium on Antennas and Propagation, Charleston, SC, June 1-5, 2009.

Appendix C: HFSS Method

Chris Johnson and Christopher Wagner
Department of Electrical and Computer Engineering, University of Idaho

Introduction

Ansoft's High Frequency Structural Simulator (HFSS) is a commercial frequency-domain, finite-element electromagnetic fields solver. The purpose of this particular investigation is to ascertain whether or not HFSS is applicable for simulating ELF electromagnetic signals. Towards that end, discussions are provided below that address how HFSS should be used and validation data are also provided to substantiate the efficacy of HFSS for this application. It is assumed in this discussion that the reader is already familiar with the use and operation of HFSS; this report only focuses on those features of HFSS that are unique to ELF signal generation and data processing. Version 11.1.3.1 was used in the following discussion.

Using HFSS

Hertzian Sources

The Hertzian dipole is a source option available under the excitations menu in HFSS. Per equivalence theory, this source is capable of producing the fields of an electric or magnetic dipole. To implement this source, the following needs to be executed:

1. Select "Excitation/Assign/Incident Wave/Hertzian-Dipole Wave"
2. Specify the location of the source in the model.
3. Select the dipole moment and dipole direction "Cartesian/Spherical Vector Setup" tab.
4. Select the "Hertzian-Dipole Wave Options" tab.
5. The next tab has two options: the radius of surrounding sphere and type of dipole.

The first option needs a bit of clarification. It allows the user to specify a mathematical spherical surface that surrounds the dipole. On this surface HFSS impresses a set of equivalent currents that produce the same field as that of a dipole. Although equivalence theory does not restrict the size of this sphere, the size does impact the simulation efficiency. A small sphere requires smaller tetrahedrons and for a given domain size, this implies more tetrahedrons and longer simulations. Larger spheres imply just the opposite, but preclude examination of the fields close to the dipole, since one cannot ascertain field information within the sphere. Thus a tradeoff between spherical size, computational efficiency and computational accuracy is

required.

For ELF applications we found that a sphere of 10 meters does not cause a substantial increase in computation time and allowed sufficiently close observations for most applications. If a study of the effects within the 10 meters is necessary then a second model can be created with a much reduced domain so that the computation time does not become extremely burdensome. Note: HFSS places restrictions on the size of the objects and domains with respect to the default units of the model. For example, HFSS does not allow the use of millimeter sized objects when dealing with kilometer sized domain and vice versa. The default model units can be changed under "Modeler/Units" in the main menu. It should be set to "km" for most ELF applications.

Edit Source menu

HFSS has an option that allows the user to change how the fields are calculated during the post processing step. Under the tab HFSS\Fields\Edit Source there is an option for total field or incident field calculations. This has no effect on how the fields are calculated during the solution process but does affect how the information is presented. For example, the scattered fields formulation is recommended when dealing with plane waves, but it can lead to errors when the total field is weak, which suggests that the incident and scattered field are roughly similar. That is, the subtraction of the incident field from the total field yields a small number that is susceptible to numerical noise. This error is particularly pronounced in a vacuum where the total is zero. The results in this paper were all done with the total fields option selected.

PEC Block Excitation

The Hertzian sources in version 11.1.3 are not implementable when the source is embedded in lossy media. For this reason there was considerable doubt early on about whether HFSS was a viable tool for this project. Upon further investigation and consultation with HFSS technical support a solution to this problem was found. It was discovered that an equivalent source can be constructed using a perfectly conducting block of any shape. This is accomplished by implementing the following steps:

1. Place a perfect electric conductor (PEC) volume where the source is to be placed.
2. Embed a Hertzian electric dipole or magnetic dipole in the block.
3. Place a radiation boundary that encompasses the block using the "Incident Field" specification.
4. Make sure the surrounding sphere of the Herztian source is completely contained within the PEC block.

We surmise that this approach is in effect using a scattered field formulation by impressing an incident field on the block and allowing the block to scatter that field. The scattered field is equivalent to that of a dipole. This approach does cause a scaling factor to be introduced in the data that is still under investigation.

Boundary Conditions

As with any full domain solver that is simulating fields within an open domain, care must be taken to truncate that domain with a radiation boundary condition that emulates an infinite space. HFSS allows the user to choose between a low accurate radiation boundary condition or a highly accurate perfectly matched layer (PML). The radiation boundary and the PML boundary are both available under the "Boundaries" menu. We have found that both conditions work quite well for ELF applications. Due to the simplicity, we typically use a radiation boundary and have found that default settings are sufficient.

Global Materials

The global material setting (typically a vacuum) is the default material when no material is selected by the user. However, the global material setting also impacts the quality of the radiation boundary, particularly when observation points are chosen that are close to the radiation boundary. HFSS recommends that the global material setting be that which is specified for the interior. For example, in the case of an antenna radiating in a vacuum, the global material setting should be a vacuum; if it is radiating in water, then the global material setting should be water, etc. However, in a multilayered or inhomogeneous material, there is no one global material setting that is optimal. To obtain the best solution, however, HFSS recommends that the global material setting be that of the material that surrounds the observation point. As an example, consider a three-layered region of air, water and mud. If the observation point is in air and close to the radiation boundary, a global material setting of air should be used; if the observation point is in mud and close to the radiation boundary, a global material setting of mud should be used, and so forth. To set the global material:

1. Select the model
2. Select "HFSS/Boundaries/Edit Global Material Environment"

Mesh Surfaces\Volumes

A high-quality mesh is critical in obtaining good results from HFSS. A sophisticated meshing tool is embedded within HFSS that automatically meshes the problem space based on the input from the solid modeling editor. However, as with any meshing tool, the resulting mesh is not always optimal. For this reason it is sometimes critical to

guide the meshing tool by adding non-material surfaces that assist the tool to place more (or less) tetrahedrons within a given area in order to improve accuracy (i.e. more tetrahedrons) or to increase computational speed (i.e. less tetrahedrons). For example, to improve the mesh along a field monitoring line, a rectangular sheet can be placed such that the edge of the rectangle is on the line of measurement. Then by performing a mesh operation on the rectangle, the user can increase the number of tetrahedrons in that localized area without significantly increasing them throughout the entire volume. These mesh operations are available in the project manager menu.

Exporting Field Data

Exporting field data is accomplished using the "Fields Calculator" in HFSS. It is located under HFSS\Fields\Calculator within the main menu. Although numerous options are available in the Fields Calculator, only a few are relevant for this application.

In the upper right corner of the Fields Calculator is where the specific solution set of interest is specified. Take care to make sure that each parameter is set properly to ensure a valid simulation, per the procedure below:

1. Generate a solution using the "Analysis" option under the project manager tree.
2. The "Solution" drop down menu has all the different solutions that were generated by HFSS
3. After the solution is selected then any field type, frequency data, or phase data that has a saved solution can be selected.
4. If a parametric sweep was done then the different parameters can be selected with the "Change Variable Value" button.

After specifying the solution of interest, the values of interest need to be specified.

5. Select the "Quantity" button. When it is selected a drop down menu will appear and E and H values can be selected. When either is selected an entry will appear in the command queue area.
6. Select the "Export" tab. This will cause another GUI to appear.
7. In the first empty field type the name of the exported file.
8. Select the point where you want the Fields Calculator to compute the fields in the model. There are two ways to do this. First is to have HFSS calculate the locations by specifying the start point, end points and spacing. The second way is to create a tab delimited file with the suffix of *.pts and import the points. The file should have no column header, should have the columns arranged in x, y, z order and should be in units of meters.
9. After selecting "ok", HFSS will export a file with the field data.

Near Field Line Setup

The near field line setup is an option in HFSS that allows the user to solve for the near fields along a line. It can be any polyline of one or more segments. It is necessary to have the near field line setup to measure values along a specific line such as a radial line leading away from the source. Before near field data can be plotted or exported a setup must be defined. This is done in the "Radiation" option in the project manager.

1. Select a line or lines that you wish to use.
2. Select "Radiation/Insert Near Field Setup/Line." A new window will appear with a couple options to select.
3. Specify the name of the set-up.
4. Select what geometry is desired for the set up. If the right line was not initially elected, it can be selected now.
5. Input the number of evenly spaced points that will be calculated along the geometry.
6. All other options should be left as default.

This process can also be used to get points to use in the fields calculator. By right clicking on the setup for the geometry of interest, select "Compute Max Parameters." A new window appears and gives several options to choose, in particular the solution to use and the frequency. Select "ok" to continue. HFSS will do some calculation and another window will appear giving a summary of the near field values to be exported. Select "Export Fields" and a *.csv file will be created that will contain points along the line and field values. This file can then be opened in excel and edited to meet the format required for the fields calculator by deleting the headers, index, and field values so that all that is left is the *x, y, z* points. Save the file as a tab delimited file and change the file suffix to "*.pts."

Validation

The following discussion hinges on the validation of HFSS data. The actual electromagnetic phenomena associated with this data are of secondary importance.

- Figures 1 and 2: The first validation scenario considers a 1,000 Hz electric source in homogeneous, lossy water with a conductivity of 0.018 S/m. Data generated by HFSS and by the standard electric dipole solution are plotted and compared. The correlation between data sets is quite good, but a calibration multiplier of six was needed in the HFSS data. The reason for this factor is not readily apparent to us, but further studies performed by us have suggested that the factor is proportional to $f^{1/2}$. Since the wave number is also proportional to $f^{1/2}$ in lossy media, we surmise that the calibration factor is related to wave

number.

- Figures 3 and 4: The second validation scenario considers a 100 Hz source in free space. Data generated by HFSS and by the standard electric dipole solution are plotted and compared. Although the electric field comparison is quite good, the magnetic field comparison is not. The trend in the magnetic field is correct, but the HFSS data is sporadic about the trend line. Since HFSS is an electric field solver, this sporadic data is associated with the post-processing step that converts electric field data into magnetic field data via Ampere's law. The quality of the magnetic field data is improved by mesh refinement, since the mesh dictates the quality of the numerical derivatives. In addition to this issue, a multiplication factor of sixteen was needed to get the HFSS data to agree with the standard dipole solution. The need for this factor is still unknown.
- The data of Figures 6, 7, 8 and 9 are associated with the three layered-geometry of Figure 5. The conductivity of the water is 0.018 S/m; the conductivity of the floor is 0.012 S/m. For Figures 6 and 7, the excitation is of the electric kind; for Figure 8 and 9, the excitation is of the magnetic kind. The operating frequency in both cases is 1,000 Hz. In both cases the source and observation points are located 11 m below the surface and 5 m below the surface, respectively. In all four figures, the correlation between the HFSS data and the Sommerfeld (WSU) data is quite good. Again, however, a multiplication factor is needed in the HFSS data to obtain good correlation. In the case of Figures 6 and 7, the factor is six; in the case of Figures 8 and 9, the factor is sixty. Further research is needed to understand and to quantify this factor.

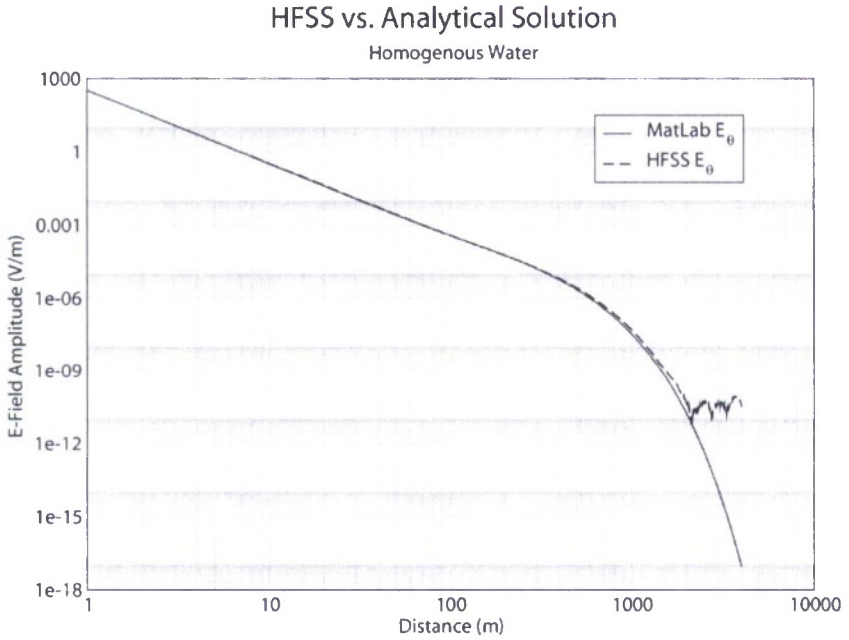

Figure 1

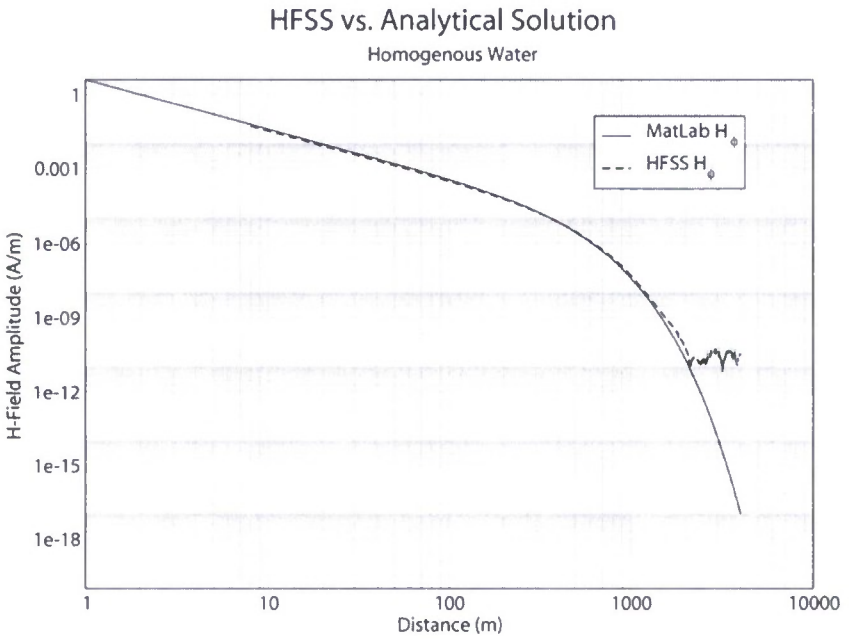

Figure 2

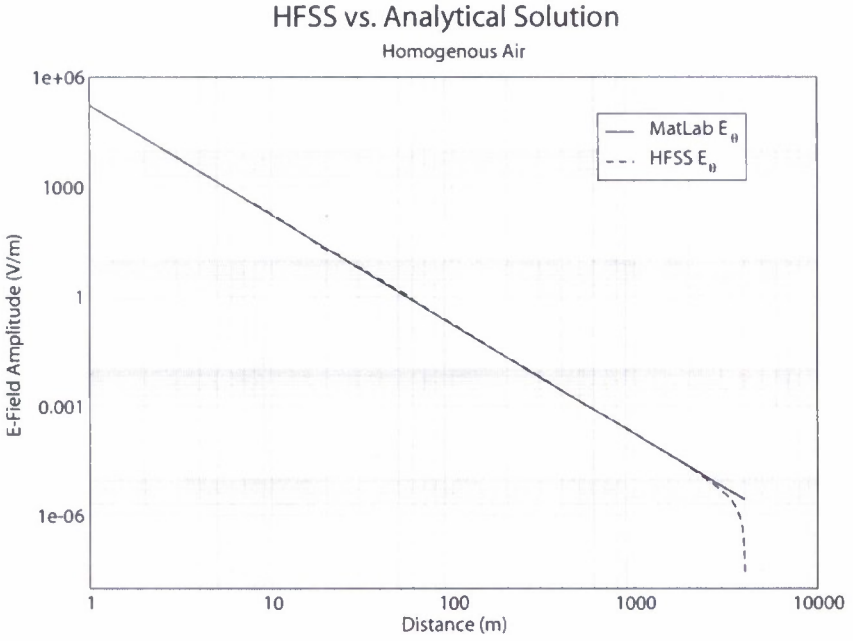

Figure 3

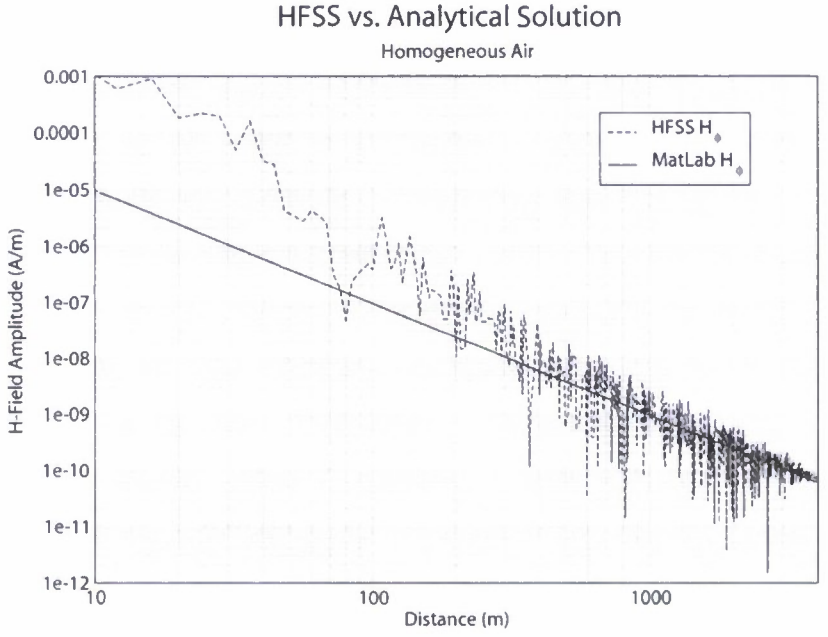

Figure 4

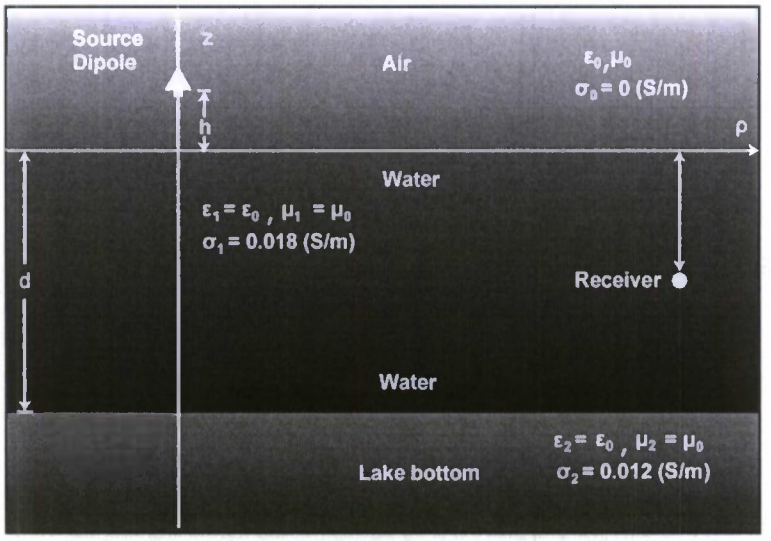

Figure 5: A depiction of a flat, three-layered Lake.

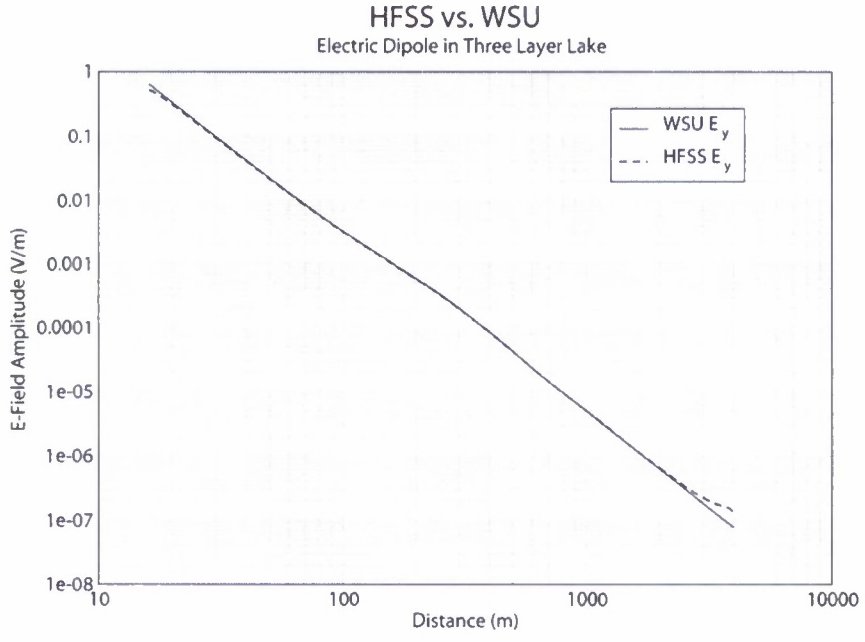

Figure 6

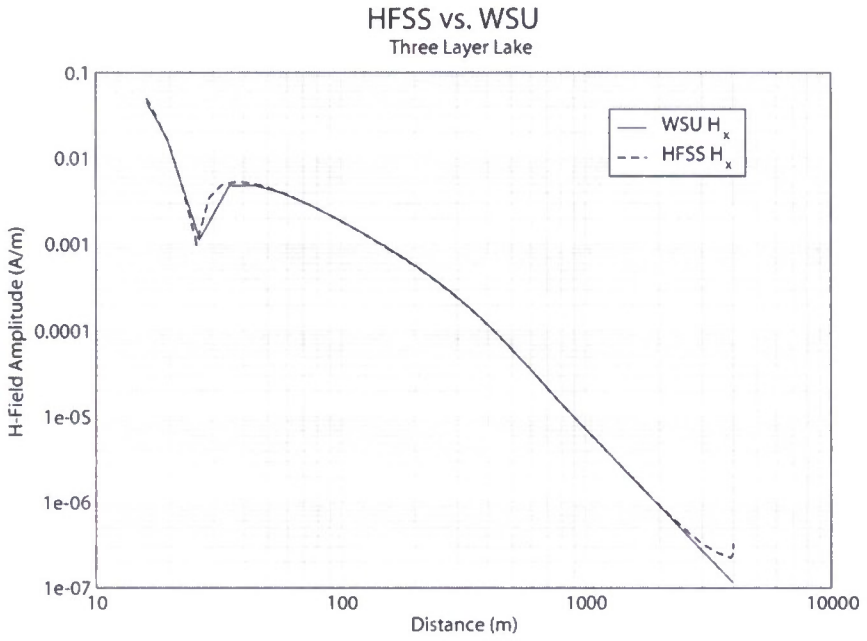

Figure 7

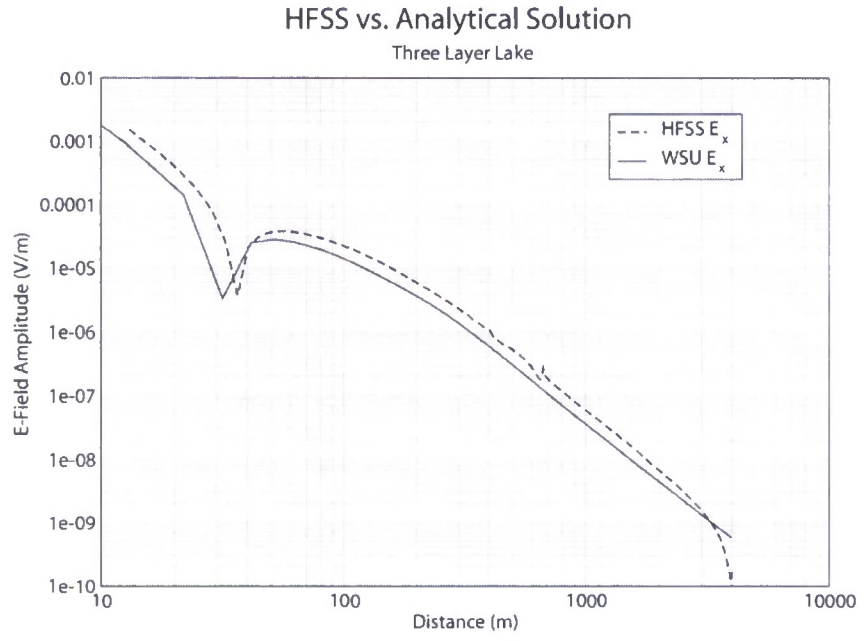

Figure 8

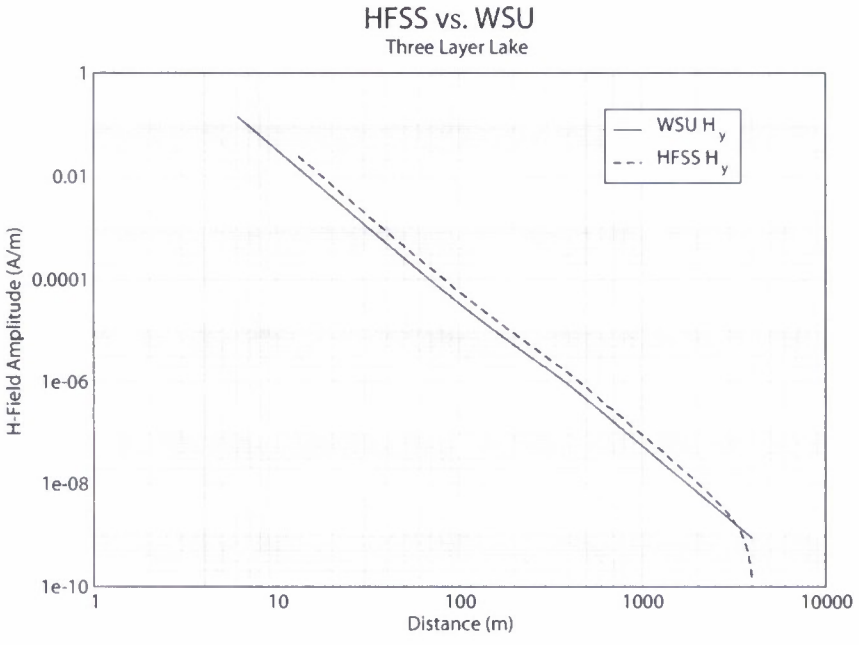

Figure 9

Future Work

It is clear from the preceding discussion that HFSS is indeed a viable tool for computing ELF signals in water. However, there still exists several issues that need to be resolved to make this tool highly effective. These are:

- Multiplication Factor: As noted in the previous data, a frequency-dependent multiplication factor is needed to get correlation between the HFSS data and the closed-form solutions. The reason for this factor is not understood and needs to be investigated.
- Electric Field Excitation, Magnetic Field Observation: When an ELF electric source is used to excite a magnetic field, the corresponding magnetic field data in HFSS follows the correct trend, but the data is still nevertheless quite sporadic. We believe that this issue is directly related to the mesh. Some kind of mesh refinement is believed to be needed to resolve this problem.
- Meshing: Given that the Lake has regions where the floor and surrounding landscape spatially varies in large amounts and has other regions where such variations are little, the finite-element mesh needs to be optimized to obtain both rapid and accurate solutions. A meshing software package has been purchased to assist HFSS with the meshing process. Use of this package will be a key activity of Phase Two.

- Computer Resources: HFSS is a computationally intensive program. Its ability to solve large, complex probelms is directly linked to the available computer resources. In the case of this ELF project, a resource study will be conducted to ascertain the required computational resources that HFSS will need to accomplish the stated tasks.

Appendix D: Quasi-Static Method

Robert Rebich and Christopher Wagner
Department of Electrical and Computer Engineering, University of Idaho

Introduction

For ELF frequencies, the corresponding wavelengths are very large compared to the domain size, which suggests that wavelike motion is not a main attribute of the electromagnetic field. Therefore an electrostatic solution can be applied to approximate the fields. For a system to be regarded as quasi-static the time rate of change in the electric field is negligible for magnetic source excitation; the time rate of change in the magnetic field is negligible for electric source excitation. This allows us to write electric field solutions in terms of a scalar potential and magnetic field solutions in terms of a vector potential. In this work, we have only concerned ourselves with quasi-electrostatic (QES) effects.

The QES system is shown in Figure 1. The materials that define the two layers are characterized by their conductivity and permittivity. The experiment took place on a lake; therefore the two material media model will be air and water with their corresponding material characteristics shown in the figure. The green dots in the water represent a set of electrodes with opposite charges and the green dots in the air represent the images electrodes. The image electrodes produce the same fields at the EMA that the reflected fields off the interface from the original electrodes. The electrodes are located at a vertical distance h from the interface and separated by a distance d. The red dot represents the EMA (x, y, z). The model replicates the experiment by moving the electrodes along a radial axis and measuring the fields at the EMA.

To energize the electrodes, a voltage V is impressed between them. The experimental voltage between the electrodes is unknown, but the current was recorded. To find the voltage, we estimated the impedance between the electrodes and multiplied that impedance by the current.

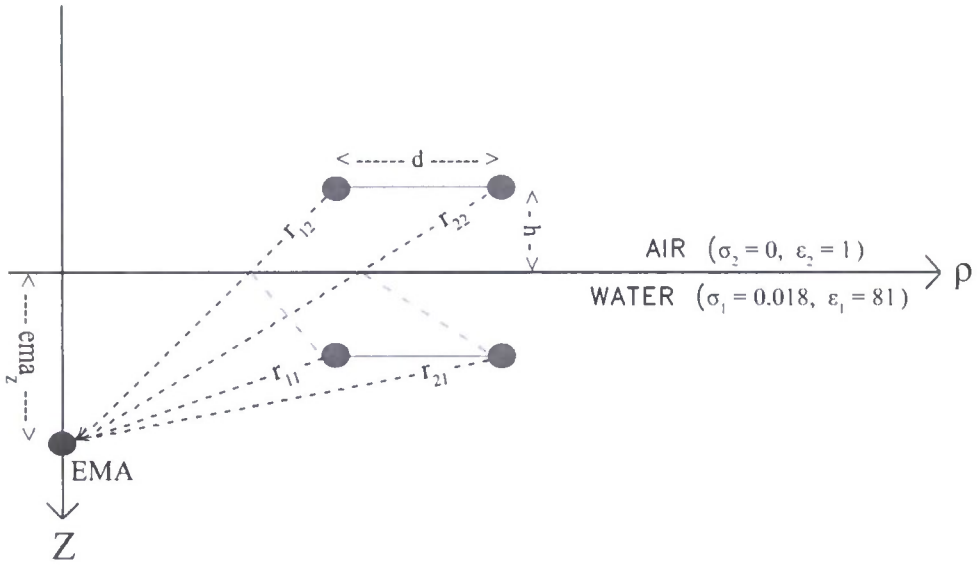

Figure 1: Geometrical rendition of the quasi-static geometry.

The voltage can be determined anywhere in the domain by a simple electrostatics relationship. The total voltage is the superposition of each contribution made by each of the real and image electrodes. The voltages in the water and air are given as,

$$V = \frac{j\omega q}{4\pi(\sigma_1 + j\omega\varepsilon_1)}\left[\frac{1}{r_{11}} + \frac{R}{r_{12}} - \frac{1}{r_{21}} - \frac{R}{r_{22}}\right], \qquad Z > 0$$

$$V = \frac{j\omega q}{4\pi(\sigma_1 + j\omega\varepsilon_1)}\left[\frac{T}{r_{11}} - \frac{T}{r_{21}}\right]. \qquad Z < 0$$

Here R is the reflection coefficient at the interface and T is the transmission coefficient at the interface. The posistion vectors are functions of x, y and z and are as follows:

$$r_{11} = \sqrt{\rho_1^2 + (z - z_1)^2} \quad r_{12} = \sqrt{\rho_1^2 + (z + z_1)^2} \quad \rho_1 = \sqrt{(x - x_1)^2 + (y - y_1)^2}$$

$$r_{21} = \sqrt{\rho_2^2 + (z - z_2)^2} \quad r_{22} = \sqrt{\rho_2^2 + (z + z_2)^2} \quad \rho_2 = \sqrt{(x - x_2)^2 + (y - y_2)^2}$$

The subscripted coorrdinates refer to either the first charge (left) or the second charge (right). Once the position vectors and potentials are known, the total electric field can be determined through the gradient of the voltage:

$$\boldsymbol{E} = -\nabla V$$

The validity of the code is based upon the assumption that the charge on the spherc is uniformly distributed. This assumption will fail when the two spheres are close to each

other or when the spheres are close to the material interface.

A comparison of the QES solution versus experimental and other solution methods is shown in Figure 2. The dipole for the experiment was oriented down the positive x-axis, which resulted in a very weak component of E_y; therefore only E_x (solid curves) and E_z (dashed curves) are represented. The plot shows very good comparisons for the QES and Sommerfeld (WSU) solutions. After about 100 m the WSU E_z component flares away from the QES E_z. This is expected since the QES solution cannot account for wave-like effects, unlike the WSU solution. The experimental data from run #1117 are also comparable to known analytical solutions. The characteristics of the curves matched the characteristics of the analytical solutions.

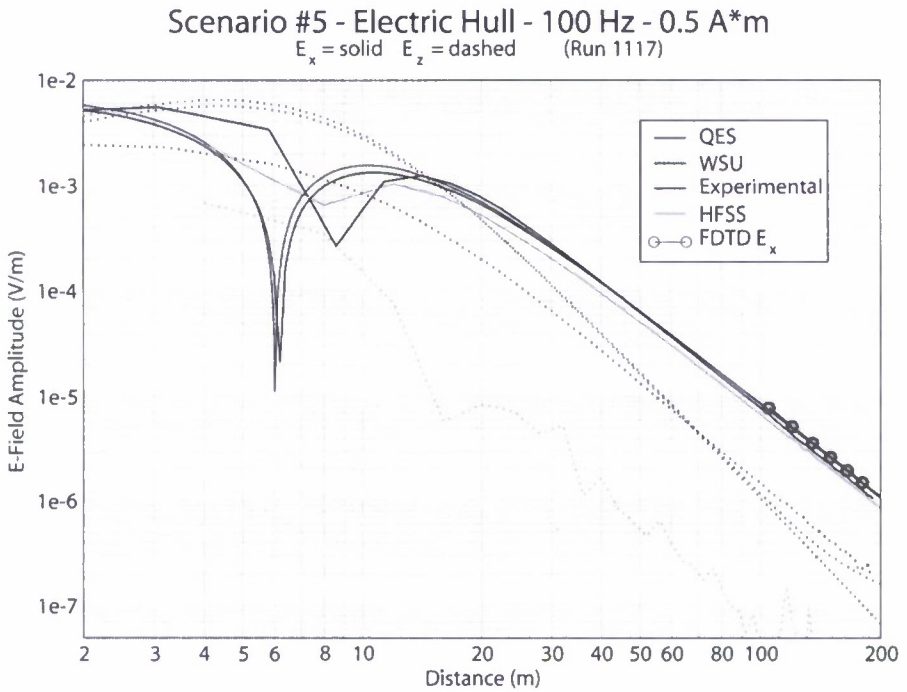

Figure 2: Field comparison for Run #1117. Source is 0.5 A-m.